EXPERIMENTAL STUDY OF EFFECTS OF LEADING-EDGE STRUCTURES ON THE DYNAMIC STALL OF A VERTICAL AXIS WIND TURBINE AIRFOIL

A Thesis
Submitted to the Graduate Faculty
of the
North Dakota State University
of Agriculture and Applied Science

By

Jiaming Zhao

In Partial Fulfillment of the Requirements
for the Degree of
MASTER OF SCIENCE

Major Department:
Mechanical Engineering

December 2019

Fargo, North Dakota

North Dakota State University
Graduate School

Title

EXPERIMENTAL STUDY OF EFFECTS OF LEADING-EDGE STRUCTURES ON THE DYNAMIC STALL OF A VERTICAL AXIS WIND TURBINE AIRFOIL

By

Jiaming Zhao

The Supervisory Committee certifies that this ***disquisition*** complies with North Dakota State University's regulations and meets the accepted standards for the degree of

MASTER OF SCIENCE

SUPERVISORY COMMITTEE:

Dr. Yan Zhang
Chair

Dr. Y. Bora Suzen

Dr. Jordi Estevadeordal

Dr. Huojun Yang

Approved:

4/20/2020
Date

Dr. Alan Kallmeyer
Department Chair

ABSTRACT

Vertical axis wind turbine, developed as one of the main methods to utilize the wind energy, has a promising future; however, the major issue to limit its performance is the uneven loading on the blade during operation. Flow control mechanisms have been employed in the aerodynamic field to improve the performance of airfoils. In this study, two types of leading-edge structures, including flexible leading-edge and leading-edge roughness, are experimentally investigated to analyze their effects on altering the aerodynamic characteristics of NACA 0018 airfoil under steady flow condition and dynamic pitching condition. Current experimental results indicate that 1) during the steady flow condition, both of leading-edge structures contribute to the delay of the static stall; 2) for the dynamic pitching process, the leading-edge structures either delayed the dynamic stall angle or increased the area of the coefficient of pressure loop as a function of angle of attack.

ACKNOWLEDGEMENTS

I would like to express my sincere gratitude to those who supported me and made this thesis possible. I would like to thank the Mechanical Engineering Department at North Dakota State University for the financial support during my study and research. I am very grateful to my Graduate Advisor, Dr. Yan Zhang for his enthusiasm, patience, and support. His advice helped my professional and personal development I would also like to thank the members of my Graduate Advisory Committee, Dr. Bora Suzen, Dr. Jordi Estevadeordal and Dr. Huojun Yang, for their helpful advice and suggestions. I especially wish to thank my Dad and Mom for their encourage and support, and to thank my friends especially Ruihang and Habib, for their support and encouragement.

TABLE OF CONTENTS

LIST OF TABLES

LIST OF FIGURES

1. INTRODUCTION

Wind energy is one of the major renewable energy sources as it generates 6.5% of the nation's electricity in 2018, claiming the largest source of renewable generating capacity in the US [1]. The American Wind Energy Association reports that wind energy, in 2016, contributes greatly in Midwest and Great Plains' electricity needs: 35% of Iowa State and 30% of South Dakota. For other states, for example North Dakota and Oklahoma, more than 20 percent of their electricity demand is produced by wind energy [2]. Wind energy has some unbeatable advantages playing a determine role in present market:

- Wind energy is a sustainable and abundant energy source, generated by the temperature difference of the atmosphere or irregular earth's surface. The nation's cumulative wind power capacity has an average 30% increase annually over the past decade.
- It is a clean, non-polluting energy. Wind turbines extract the kinetic energy from the wind and do not emit any pollutants or greenhouse gases.
- Wind power is cost-effective. Land-based wind energy claims of the cheapest energy sources, costing around two to six cents per kilowatt-hour. Unlike traditional sources of energy, wind energy mitigates price uncertainty due to free fuel [3].

The earliest recorded history of utilizing the wind power could be tracked back to 5,000 B.C., people used the wind energy to propel the boats along the Nile River. Later, windmill was invented in eastern Persia and spread to the Middle East for food production. These wind energy technologies eventually spread to the European countries around 1,000 A.D. to help drain the lakes and was developed for commercial use, such as pumping water and generating electricity, in the United States in nineteenth century [4].

Nowadays, a total of 57,636 land-based commercial wind turbines have been employed in 2018 nationwide [5]. Industrial wind turbines fall into two general classes depending on how the turbine spins horizontal axis wind turbine (HAWT) and vertical axis wind turbine (VAWT). Horizontal axis wind turbine has the main rotor shaft arranged horizontally and electrical generator at the apex of the tower and must be pointed in the direction of the wind to be effective. On the other hand, the vertical axis wind turbine has the vertically located main rotor and does not need to be pointed in the direction of wind. Hence, it has a better performance than the horizontal axis wind turbine in the situation where the wind direction is highly uneven [6].

1.1. Vertical axis wind turbine (VAWT)

To date, HAWTs dominate the commercial market due to the efficiency of generating the wind power. Many academic studies have been focused on the HAWTs. However, the research and design of VAWT were carried out by the USA Department of Energy, Sandia National Laboratories in late 1970s and early 1980s. It is believed that VAWTs will have the potentials to reemerge in the future wind energy market, particularly related to offshore wind applications. In 2011, the Department of Energy (DOE) conducted a $4.1 million five-year project for applying VAWTs for offshore wind farms. Wind energy researchers from Sandia National Laboratories evaluated the VAWTs performance on solving problems of transforming energy from offshore situation and confirmed that the VAWTs have better performance than the HAWTs for the offshore applications. They narrowed prototype of VAWTs down to a single turbine blade design (shown in the Figure 1) [7]. Furthermore, vertical axis wind turbine has some substantial advantages over HAWT at very large scale (10 MW+) which may be more appropriate in some aspects [7]–[11]:

- Suitable for the low wind speed situations

- Lower cost for construction and installation due to the ground-based gearbox
- Less land occupation
- Less sensitivity to extreme weather conditions
- Capable of withstanding high wind speed and serve wind conditions
- Installation and maintenance service can be done easily
- Good scalability to large sizes
- Better stability due to lower center of gravity

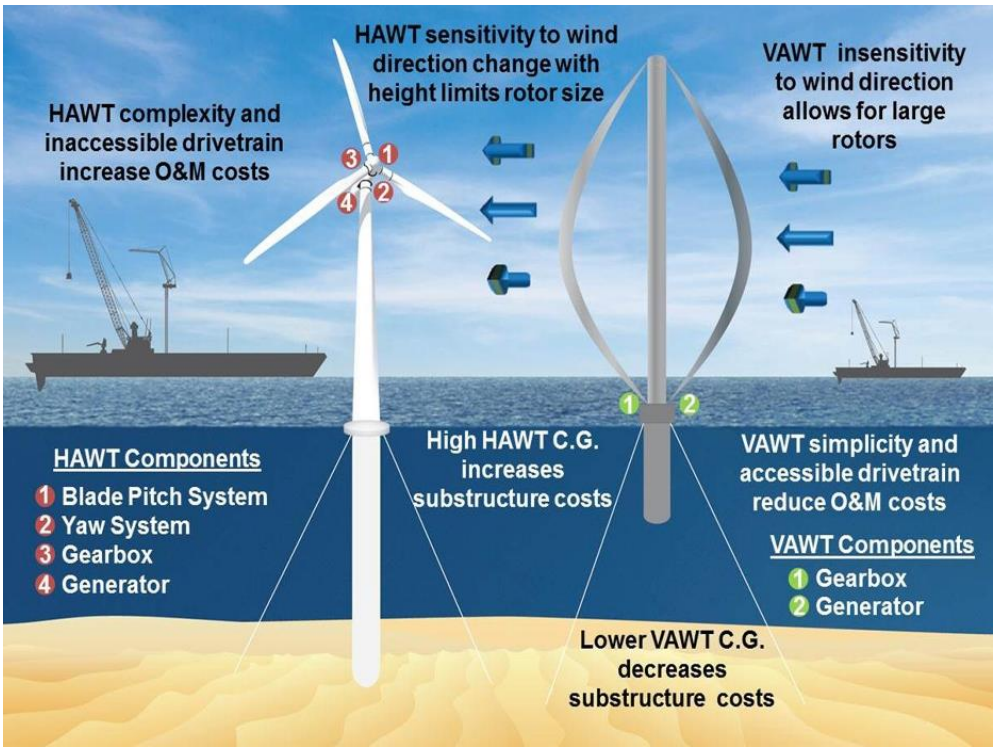

Figure 1. Prototype of VAWT for off-shore application [7].

1.2. Aerodynamics of VAWTs and the dynamic stall problem

One of the main technical barriers that hinders the commercialization of vertical axis wind turbine (VAWT) is its inherent dynamic stall and the associated low-efficiency problem. Presently, most vertical axis turbines that are employed for wind turbine applications have rigid and fixed blades. Differed from the HAWT whose blade experiences constant torque,

independently from the blade angular position, under ideal uniform wind condition, the operation of the VAWT is more complicated. The vertical-axis wind turbine generally vibrates while the change of blade angle along with the circular azimuth path (shown in Figure 2) during the rotation. This uneven variation of tangential force has the consequence of torque ripple in the output and may result in the large stress in mechanical structures as well [12]. Moreover, not all the blades produce the torque simultaneously which limits the efficiency of the VAWT. Consequently, the wind turbine structural loading pulsation lead to the early failure which is commonly observed in the industrial field [13] and also contributes the low efficiency of energy generation as the dynamic stall happens because of the rapid change of angle of attack.

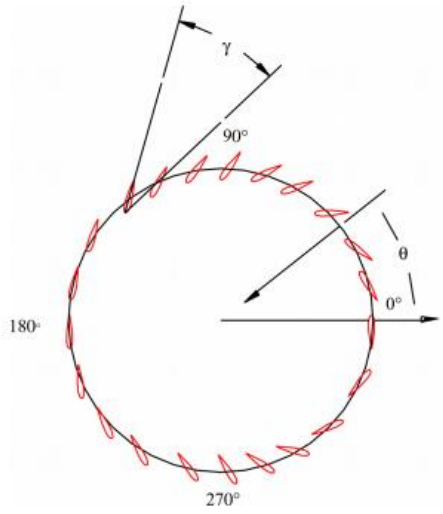

Figure 2. Circular azimuth path for VAWT [12].

Dynamic stall is one of the important factors that influence the aerodynamic behavior of the airfoil. The phenomenon of dynamic stall on oscillating airfoils would be observed while those airfoils experiencing rapid, transient and unsteady motion in which the angle of incidence surpasses the static stall critical angle, which has been studied for many years [14], [15]. As a fundamental but challenging problem in aerodynamic field, experimental and numerical analyses have been performed to understand the effects of dynamic stall on aerodynamic properties [14].

It is believed that dynamic stall has a considerable contribution on the delay of conventional flow separation on airfoils, and during this phenomenon, extra lift is generated by the leading-edge vortex, which was observed by Harris and Pruyn while the helicopter design process to explain the variation of aerodynamic properties of helicopter blades under high-speed motion [16], [17]. Some researchers investigated the formation of vortex shedding and the process which is likely influence the aerodynamic properties. Yarusevych described a laminar flow passed over an airfoil at low Reynolds number with two different results- flow separation with or without reattachment, and visualized the vortex shedding in a wind tunnel testing (shown in Figure 3 and 4) [18]. Despite of further studies on dynamic stall and its formation, dynamic stall is not fully understood in the field of aerodynamic research. Hence, research interests were gradually extended from the formation of Dynamic Stall Vortex (DSV) to factors may alter this dynamic behavior in recent decades [19]–[21]. To delay the dynamic stall to increase the performance of airfoil, the passive flow control method is introduced.

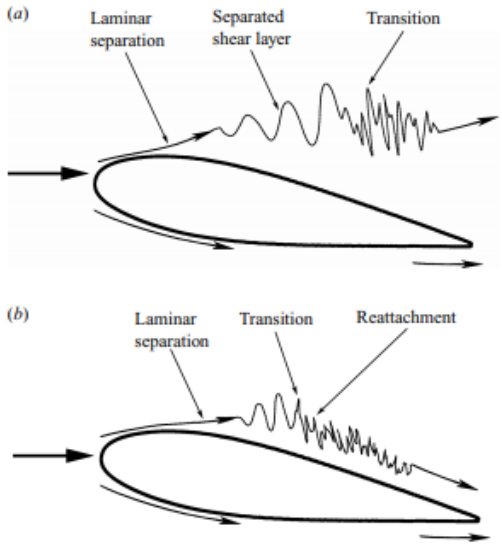

Figure 3. Flow over an airfoil at low Reynolds number: (a) flow separated without reattachment, and (b) separation bubble formation [18].

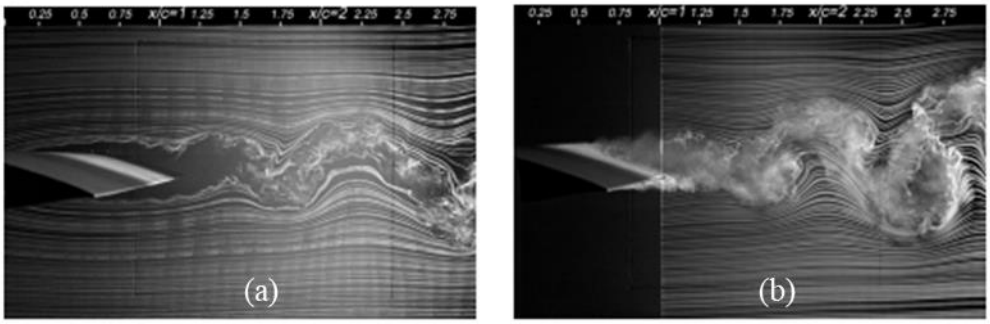

Figure 4. Visualization of flow separation at: (a) upstream, and (b) downstream [18].

1.3. Flow separation control

For the past few decades, a number of approaches for controlling the flow separation have been studies and developed in various applications, which can be divided into two kinds of flow control techniques according to their characteristics: active flow separation control techniques and passive flow separation control techniques. Generally, passive flow separation control involves geometrical modifications. They were designed to a whole-time operation regardless of need or not. Unlike passive flow separation control mechanisms, the active flow separation control is more desired in some conditions because it can be turned on or off as needed to avoid performance penalty. However, it brought extra energy into the system which indicated a higher energy may be consumed.

1.3.1. Active flow control device

Active flow control techniques were classified as the following: plasma, moving object, fluidic and others according to the Cattafesta [22]. One application of the active flow control techniques is the fluidic actuators which capable of controlling the amount of flow by fluid injection or suction. The synthetic jet is one of the mostly used fluidic actuators for modification of the lift and drag characteristics of flow. Figure 5 shows the schematic of a configuration of synthetic jet. The synthetic consists a small cavity with oscillating membrane at the bottom and

an orifice plate on its top, which can create vortices and higher momentum boundary layer by ingesting and expelling fluid into the fluid field [23].

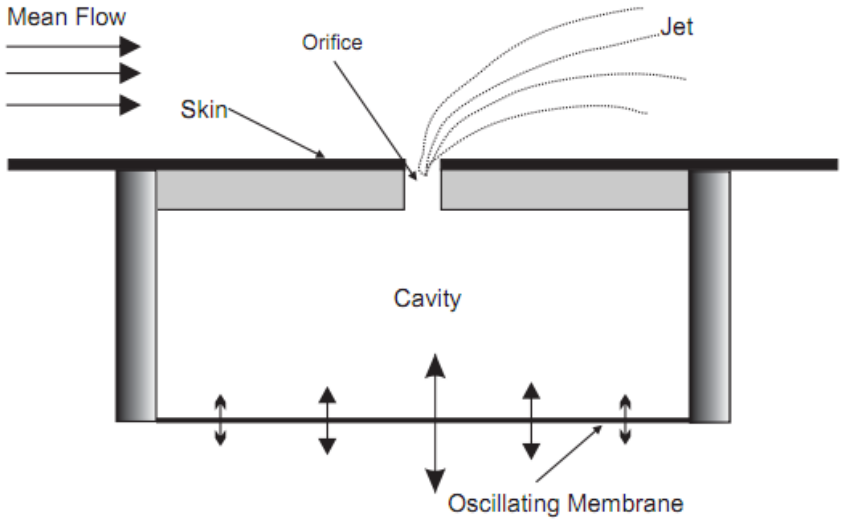

Figure 5. Schematic of synthetic jet [23].

1.3.2. Passive flow control device

For the passive flow control techniques, the vortex generators (VGs) are the most often used passive flow control device to delay flow separation in different industrial areas. Typically, they are mounted on the external surface of wind turbine blades and vehicles to achieve the goal 8 of delaying the flow separation. Despite of different design for the VGs' shape, they are generally built up as rectangular or triangular small vertical plate pointed at an angle as about the height of the local boundary layer. VGs can also be defined into many types and the Figure 6 described the co-rotating and counter-rotating types, where typically the latter shape is considered as a better solution [24]. Although the passive flow separation techniques like vortex generator are widely employed into the wind turbine blade modification to prevent the flow separation [25], [26], more research focused on the dynamic stall of VAWT airfoil with passive flow control techniques are still needed to fully understand the complex phenomena.

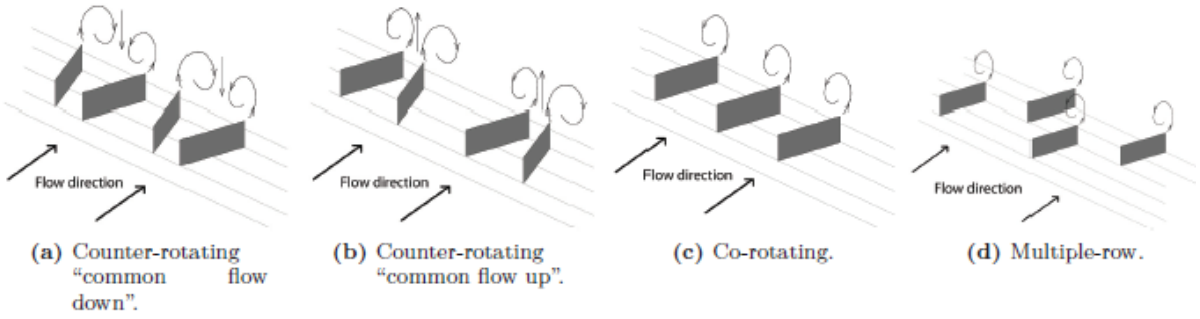

(a) Counter-rotating "common flow down". (b) Counter-rotating "common flow up". (c) Co-rotating. (d) Multiple-row.

Figure 6. Vortex generators with different setups [24].

1.4. Motivation of current study: effects of leading-edge structures on VAWT performance

Leading edge structures are commonly applied on airfoils as a passive flow control method to improve the aerodynamic properties. The objective of this study is to investigate the effects of leading-edge structures (flexible leading edge and leading-edge roughness) on altering the aerodynamic performance of the vertical axis wind turbine airfoil. The concept of using flexible material in leading-edge construction can potentially increase the turbine efficiency and reduce the operation cost and blade fatigue compared to the design of fixed rigid turbine blade [27]–[29]. According to Zeiner-Gundersen's study on a novel flexible foil vertical axis wind turbine airfoil, the blades were designed to be double cambered with fixed leading and trailing edges as shown in the Figure 7 [30]. The turbine can set up different configuration based on the specific rotational azimuth position. The fabric deformation feature enables the turbine to encounter the free stream direction at most situations to adopt more energy.

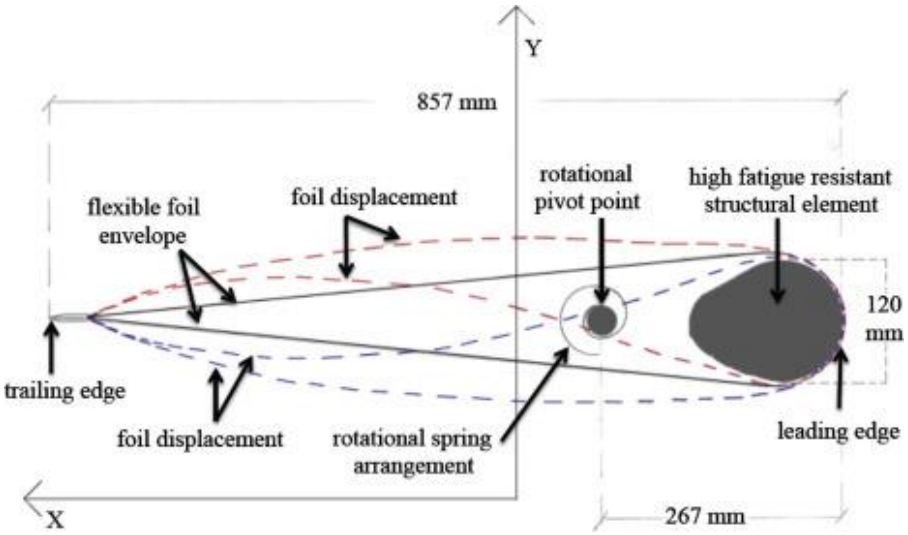

Figure 7. Double-cambered flexible profile characteristics demonstrating different cambered forms versus rotational azimuth angle [30].

For the investigation of the leading-edge surface roughness, Chakroun demonstrated the effect of various roughness on improving the lift of NACA 0012 airfoil [31]. Figure 8 shows the effects of various roughness types on altering performance of NACA 0012 airfoil in terms of lift coefficient. The results present that the airfoil with 25% wire roughness at leading-edge surface has higher lift before stalling than other cases. Table 1 below shows the experimental results as well. It could be observed that with wire roughness covering 25% of the leading-edge surface, the airfoil experienced the stall at 14° with a 0.9825 maximum lift before stalling. The stall angle was delayed by 2° than most cases [32].

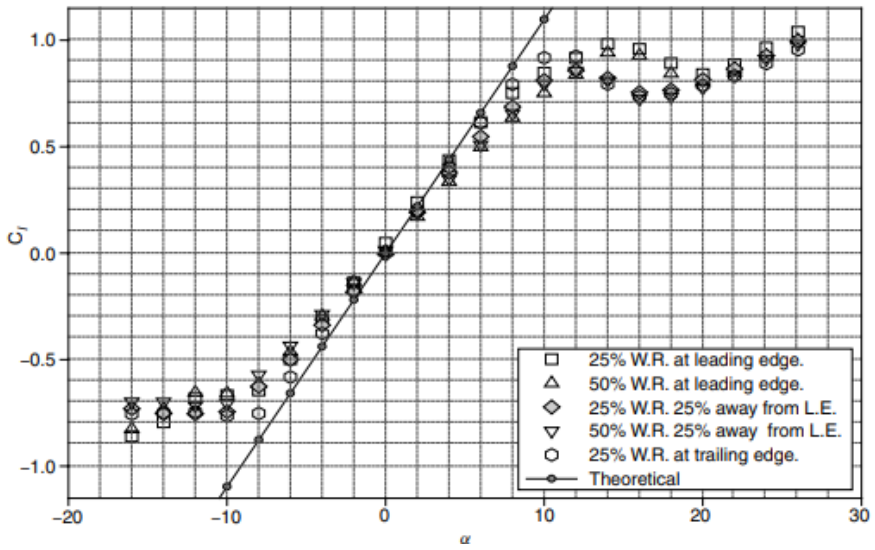

Figure 8. Lift coefficients for models with different roughness locations at Re = 1.5 *10^5 [32].

Table 1. Airfoil characteristics for airfoil models with different roughness locations [32].

Airfoil model	**Min drag**	**Max lift before stalling**	**Stall angle (°)**
Wire roughness covering 25% of airfoil surface and located at L.E.	0.04656	0.9825	14
Wire roughness covering 50% of airfoil surface and located at L.E.	0.0613	0.9422	14
Wire roughness covering 25% of airfoil surface and located 25% of chord length away from L.E.	0.0419	0.8585	12
Wire roughness covering 50% of airfoil surface and located 25% of chord length away from L.E.	0.0506	0.8556	12
Wire roughness covering 25% of airfoil surface and located at trailing edge.	0.0259	0.9247	12

1.5. Layout of the thesis

The layout of the thesis will be as follows. In chapter 2 the setup of the experiment will be discussed which includes an overview of the wind tunnel, apparatus, and the model. Further the passive flow control devices working principles and measurement techniques will also be described. Chapter 3 will give introduction of the flexible leading-edge airfoil. The experimental results will be discussed. Chapter 4 will introduce the leading-edge roughness airfoil and the experimental results. Lastly, the conclusions and recommendations for this research will be given in Chapter 5.

2. EXPERIMENTAL METHODS

2.1. Introduction

This chapter will discuss the experimental investigation methods performed on the airfoil models with the leading-edge structure modified. In the section 2.2, a pitching-motion system is introduced which enables the dynamic pitching motion of airfoils with adjustable maximum pitching angle and pitching frequency. To investigate the flow fluid, the pressure measurement and velocity measurement were involved and discussed in the section 2.3 and 2.4. To investigate the actual motion of the pitching airfoil, pictures of motions were presented in the section 2.5. The section 2.6 demonstrated the wind tunnel parameter.

2.2. Pitching-motion system

In this research, experiments are conducted under both static and dynamic scenarios. For the dynamic case, a sinusoidal pitching mechanism (shown in Figure 9) was developed to achieve the sinusoidal pitching motion of the airfoil. This system enables the airfoil performing a sinusoidal pitching motion with adjustable pitching frequency and amplitude. The small disk is driven by the motor and connected to the big disk which is employed to drive the airfoil pitching motion. This system generates the motors one-directional rotation to the oscillating motion and achieves the adjustable amplitude by altering the connecting shaft length. The reduced frequency denoted as “k” was involved in the experiment to describe the degree of unsteadiness of the airfoil pitching procedures, which is a dimensionless number. The general equation of the reduced frequency is in the form:

$$k = (\omega \times b)/V \tag{1}$$

where, ω = circular frequency, b = airfoil semi-chord, V = flow velocity. The equation of reduced frequency can be specified as:

$$k = 2\pi f c / U_\infty \quad (2)$$

where, f = pitching frequency, c = chord length, U_∞ = upstream flow velocity.

In this experiment, reduced frequencies are selected as 0.07, 0.1 and 0.15 to simulate the range of real cases of wind turbine blades motion (ranging from 0.05 to 0.15) [33].

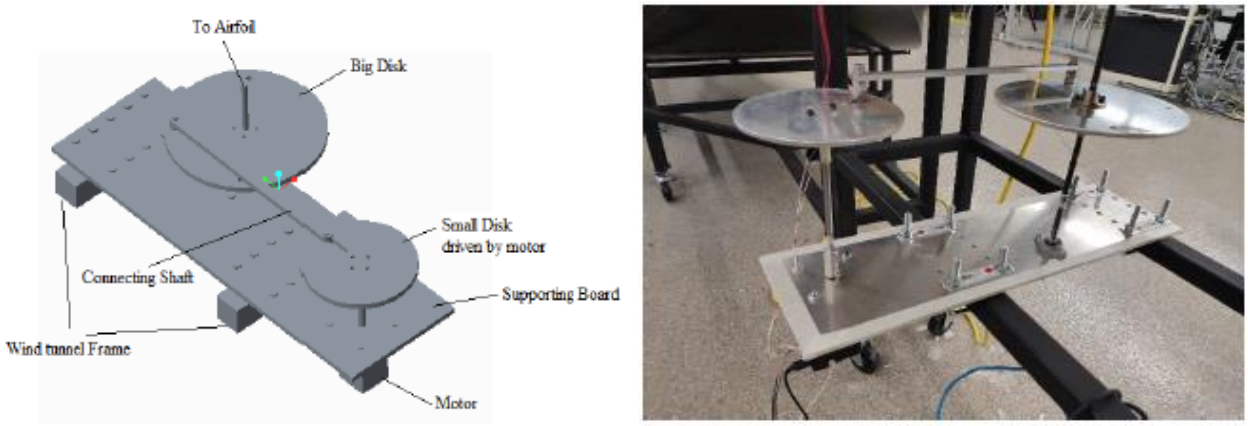

Figure 9. Dynamic pitching system.

2.3. Pressure measurement

To analyze the aerodynamic performance, surface pressure measurement was taken through wind tunnel tests. All data were obtained in the NDSU Advanced Fluid Dynamics Laboratory low-speed, 1 ft x 1 ft subsonic wind tunnel. Two different Reynolds numbers were tested in this experiment; they are 46,000 and 92,000 with associated 5 m/s and 10 m/s free stream velocity respectively. Both flexible, LE roughness, and baseline NACA 0018 airfoils were analyzed in steady flow and dynamic conditions. For the steady flow scenario, surface pressure was taken with small increments of incident angles and data were plotted for each airfoil. For the dynamic scenario, tests were performed under different reduced frequencies to analyze the dynamic stall during pitching motions (shown in the Table 2.1). All the motions were performed by pitching the airfoil from angles of attack of 0 degrees to 35 degrees and back to the starting point.

Table 2. Summary of test conditions.

Re	**k**	**Re**	**k**
46,000	0.07	92,000	0.07
	0.1		0.1
	0.15		0.15

The Scannivalve DSA 3217 pressure scanner (shown in Figure 10) was employed for the pressure collection. It has 16 standard pressure inputs and 8 true differential pressure inputs are included which can work simultaneously at 500 Hz sampling frequency. On the airfoil surface, the pressure taps were equally distributed among the upper and lower surface (for the flexible leading-edge airfoil model only) of the NACA 0018 airfoil. The terms, coefficient of pressure and coefficient of lift, were involved to analyze the pressure data, which have the form:

$$C_p = (p - p_\infty)/(\tfrac{1}{2}\rho_\infty V_\infty^2) \tag{3}$$

where, p = static pressure measured, p_∞ = static pressure in the freestream, V_∞ is upstream flow velocity, ρ_∞ is the freestream fluid density.

$$C_L = 2L/bc\,U_\infty^2 \tag{4}$$

where, L = Lift force, b = airfoil semi-chord, ρ= flow density, U_∞ is the freestream fluid velocity.

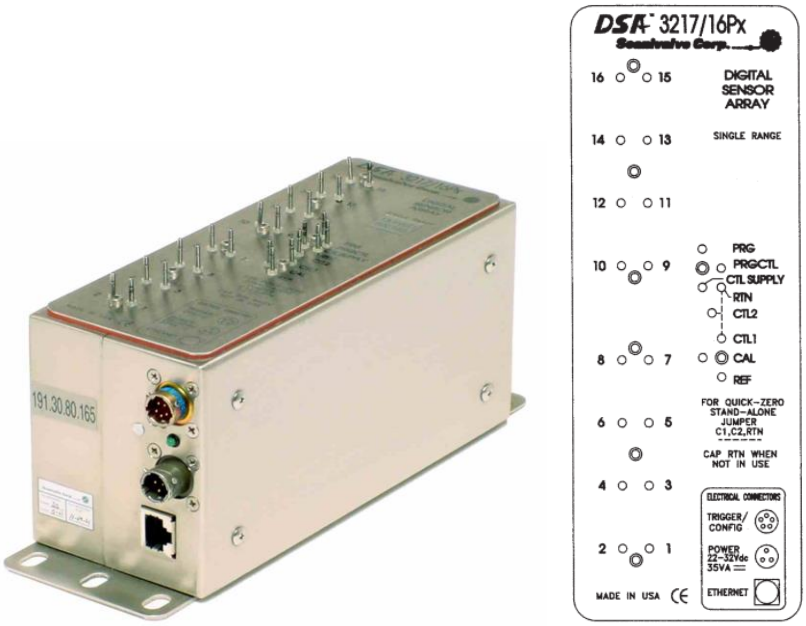

Figure 10. Schematic of DSA 3217-PTP/16Px pressure scanner and top panel.

2.4. Velocity measurement

In these experiments, the constant temperature anemometer (CTA) and the thermal anemometer sensor (model 1210-T1.5 general purpose probe) were employed to measure the velocity of the flow field by sensing the heat transfer from the element located at the head of the probe exposed to the flow (shown in the Figure 11 and Figure 12). The element was heated by the electrical current to balance the cooling effect of the flow passing by the thermal anemometer. Hence, the current would alter to hold the element at constant temperature. The change of the current reflected the variation of fluid field showing up as voltage output. The thermal anemometer was widely employed for the research study of turbulence as a standard tool due to its key feature of ability to sense the rapid change of velocity. This feature was accomplished by its fine sensing element which is as thin as four to six microns in diameter and a fast feedback circuit to shorten its time response in a few microseconds.

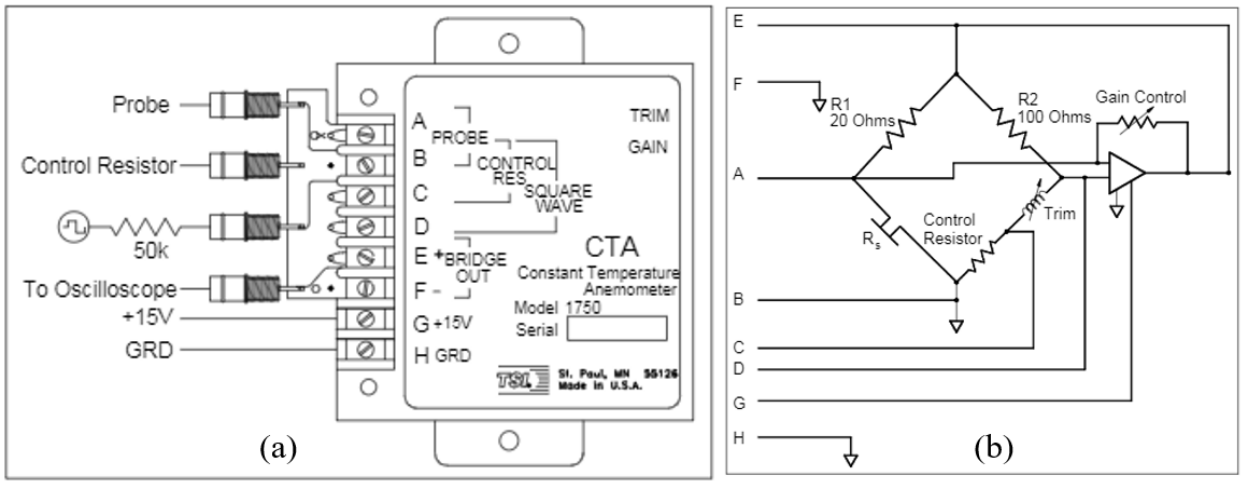

Figure 11. The schematic of (a) constant temperature anemometer, and (b) electrical block diagram.

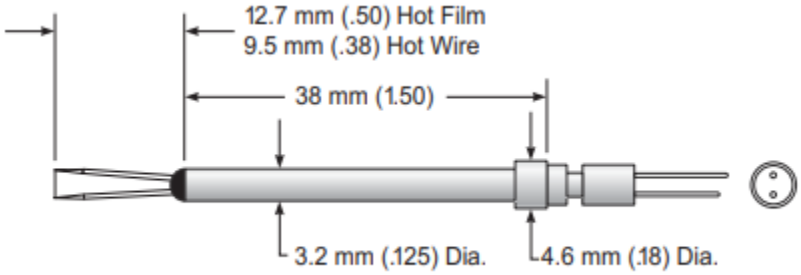

Figure 12. The schematic of model 1210-T1.5 general purpose probe.

The thermal anemometer was calibrated to convert the voltage to its corresponding velocity. The curve-fitting equation was analyzed by our research group and presented in the Figure 13 below. The velocity measurement location was shown in the Figure 14. The two locations were one chord length away from the trailing edge of the airfoil and located at midpoint of the pitching range (AoA=0°) and the maximum positive pitching angle (AoA=35°).

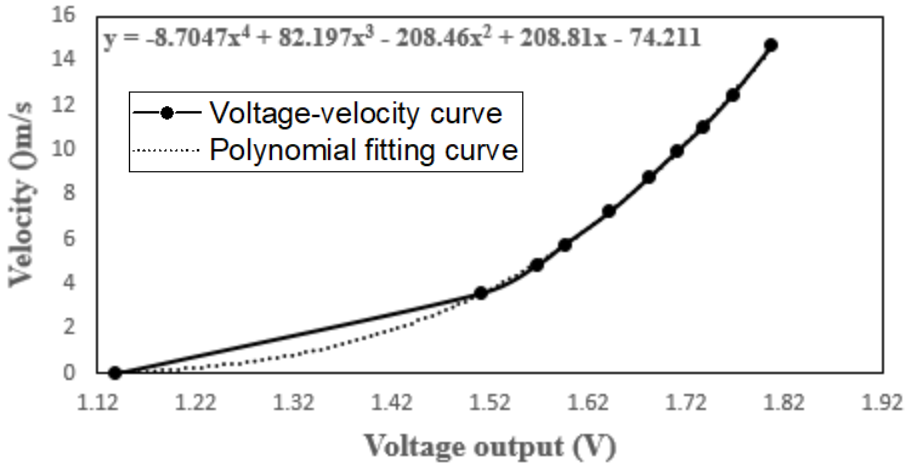

Figure 13. Thermal anemometer calibration curve.

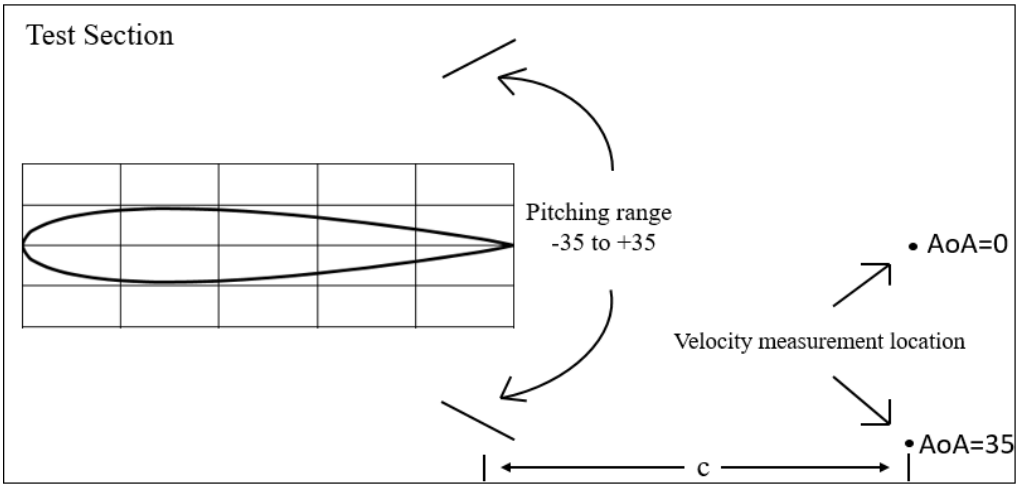

Figure 14. Velocity measurement location during dynamic pitching process.

2.5. Motion analysis

To visualize the deformation of flexible leading-edge structures for further study about the relationship between the structure deformation and dynamic stall, the FLIR blackfly high speed camera was used to catch the dynamic motion of the flexible leading-edge airfoil. It is able to capture photos or videos at a 200 Hz sampling rate with a high resolution which is 1440×1080 pixels. This camera was applied to detect record the motion of the flexible leading-edge airfoil.

Figure 15. FLIR BLACKFLY S high speed camera.

2.6. Wind tunnel parameter

The thermal anemometer was applied to examine the turbulence intensity of the wind tunnel used in this experiment for Re= 46,000 and 92,000. The Figure 16 presented the sample data for the velocity measurement of wind tunnel. It could be observed that the turbulence intensity (TI) for both cases are similar at TI =1.3%. The turbulence intensity is analyzed by using the standard deviation of the velocity data divided the average velocity:

$$TI = u'/U \tag{5}$$

where, u' is the root-mean-square of the turbulent velocity fluctuations and the U stands for the average velocity.

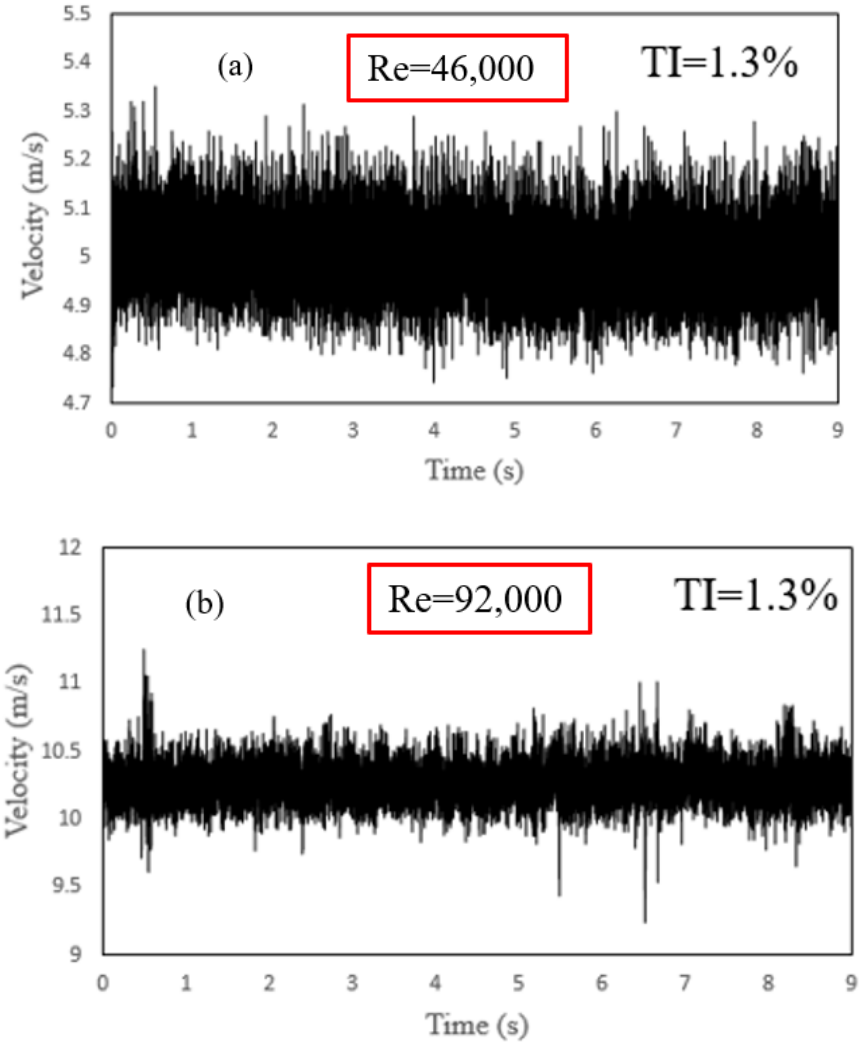

Figure 16. Wind tunnel turbulence intensity for (a) Re=46,000, and (b) Re= 92,000.

3. FLEXIBLE LEADING-EDGE AIRFOIL

3.1. Introduction

This chapter will demonstrate the experimental investigation of the flexible leading-edge airfoil model which is modified by the NACA 0018 airfoil. In section 3.2., the design parameter of the airfoil is given. The aerodynamic characteristics of the baseline airfoil and the flexible leading-edge airfoil were analyzed from section 3.3 to 3.5 for both steady flow condition and dynamic pitching condition. Finally, the section 3.6. presents some discussions on effects of the flexible structure on airfoil performance.

3.2. Flexible leading-edge airfoil model

The Figures 17 and 18 show the schematic of the flexible leading-edge airfoil model tested in the present study. The flexible leading-edge airfoil model was inspired by the Zeiner-gundersen's double-cambered flexible vertical axis wind turbine blade prototype design [30]. The most engaging feature of this tested airfoil is the simplicity of achieving the flexible portion. Different from some passive pitching mechanism techniques, the flexible portion of this airfoil was accomplished by replacing the 35% bottom leading-edge portion with flexible material-silicon rubber. During the material selection procedure, some candidates were introduced they are plastic, thermoplastic polyurethane (TPU) and silicone rubber sheet. Due to the cyclic loading conditions experienced by the blades for an extended period, considerable wear is predicted to occur. This limits the material choices to something light, yet strong and at the same time flexible and durable. TPU was chosen as the material to work with because of its flexible properties, and resistance to wear. The experimental test indicated the best performance of silicon rubber among these materials. Structural flexibility proves beneficial in the generation of lift, often increasing propulsion efficiency and energy exchange compared to steady fluid

dynamic aero- and hydrofoils. Compared to rigid or fixed foils, propulsion efficiency increases in semi-flexible flapping foils and in oscillating or moving rigid or flexible foils. The flexible leading-edge airfoil consists of blades with flexible bottoms and has the capability to change its camber in response to loads produced by air pressure during the turbine's cycle. The flexible bottom has a hollow portion (can be seen in Figure 17) in it, which help the blade induce camber when deformed. This pocket of air exists to allow the flexible surface to deform under surface pressure due to the air flow. The concept behind this prototype allows it to generate larger pressure differences at an area of maximum lift. Figure 19 demonstrates the linear deformation relationship of the silicon rubber sheet under pressure while attached on the surface of the NACA 0018 airfoil.

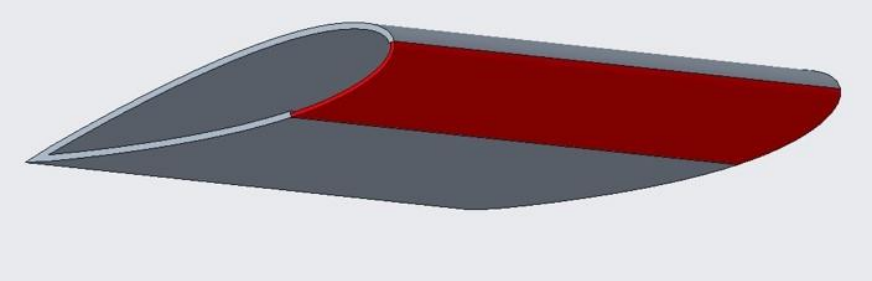

Figure 17. CAD design of flexible leading-edge airfoil (the flexible portion is demonstrated by the red surface).

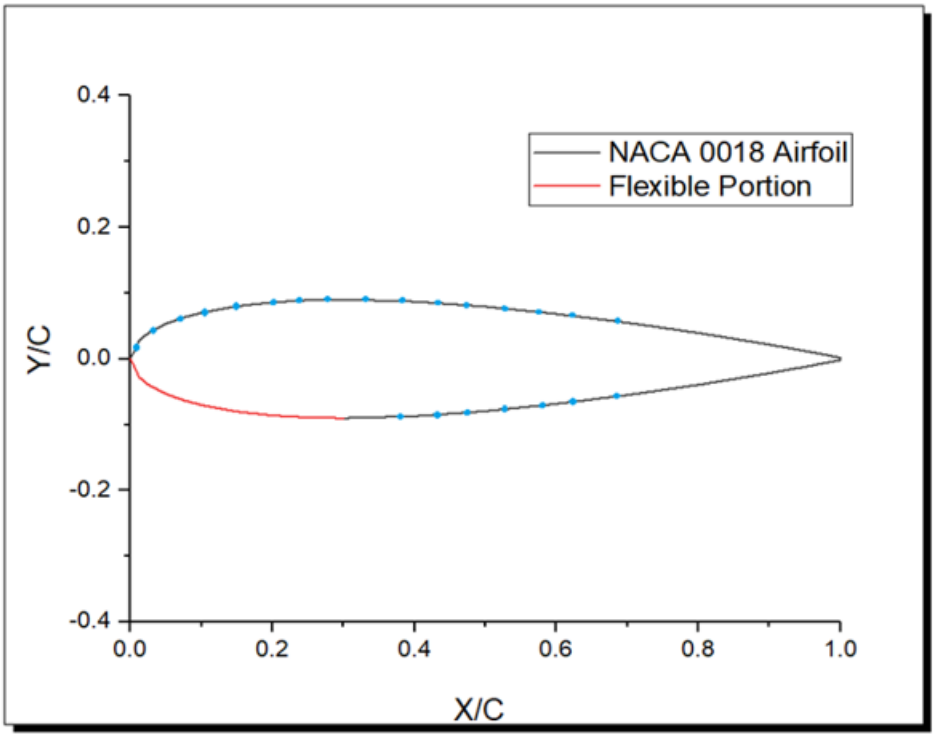

Figure 18. Schematic of the flexible leading-edge airfoil (blue dots demonstrate the pressure measurement taps).

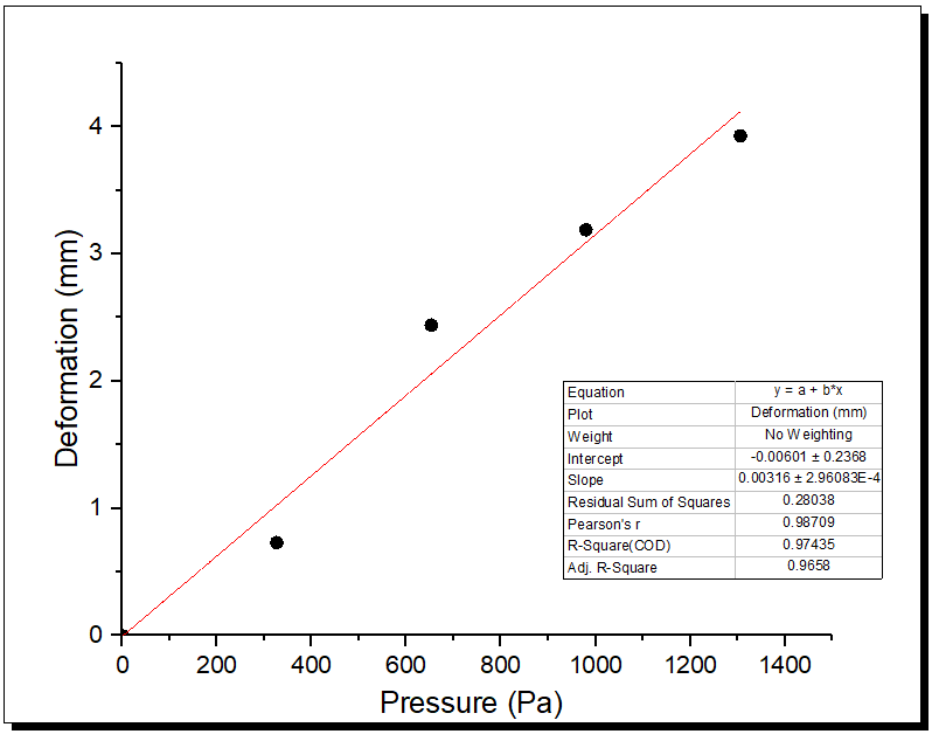

Figure 19. Maximum deformation of flexible portion under various loading.

3.3. Steady flow scenario

3.3.1. Baseline airfoil pressure distribution

The pressure measurement was performed on both upper surface and lower surface as the baseline airfoil has 16 pressure taps on the upper surface and 8 pressure taps located on the lower surface. The pressure distribution was measured to determine the changes of the baseline airfoil in different angle of attack ranging from 0 to 16 degree. Some of the angle of attacks were selected and plotted in the Figure 20 under the low Reynolds number condition. For the Figure 20 (a), it can be observed that the pressure on the suction side surface were initially increased at the small angle until 10°. A sudden drop of the pressure curves happened when the airfoil was tested under the angle of attack of 12° but the pressure curve did not become flat until 13° which suggests that the stall has occurred. The max negative coefficient of pressure was around -1.87. For the Figure 20 (b), the pressure distributions of the lower 8 pressure taps were analyzed for the selected angle of attacks, 10°, 12°, 13° and 15°. The specific locations for the lower 8 pressure taps were discussed in the section 3.2. The tendency of the pressure distribution was similar as that discussed in the Figure 20 (a). The pressure distribution on the trail edge was increased with the increment of the angle of attack until 13° where the stall has happened.

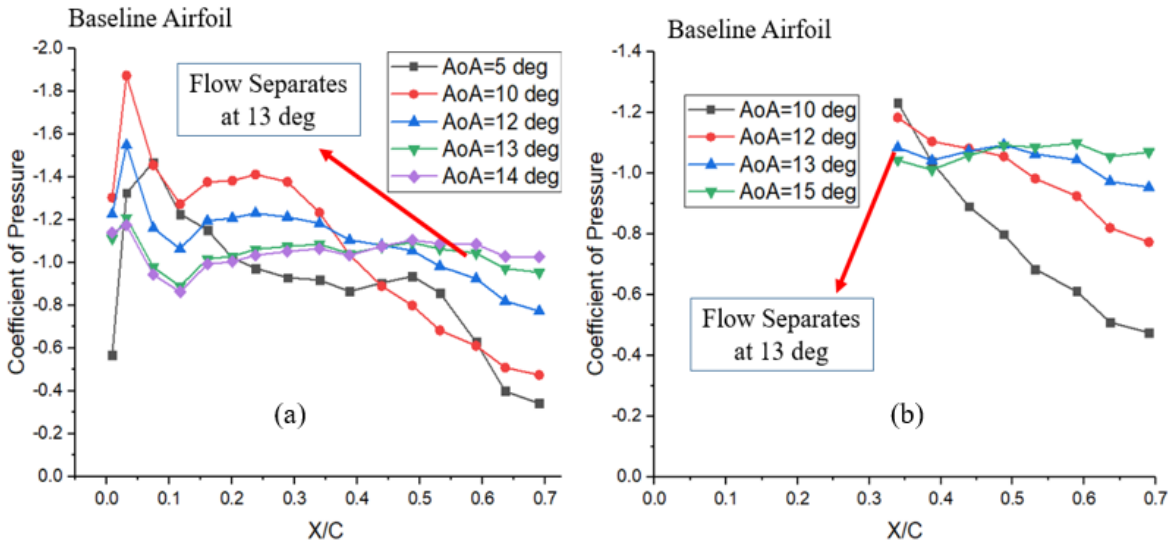

Figure 20. Pressure coefficient for the (a) rigid surface under Re= 46,000, and (b) flexible surface under Re= 46,000.

The baseline airfoil was then tested under Re= 92,000 with the 10 m/s corresponding wind speed. In the Figure 21 (a), the pressure distribution curve was observed to become flat at 15° which may suggest that the airfoil was suffering the static stall. For the Figure 21 (b), the flow separation was observed at 15 degree.

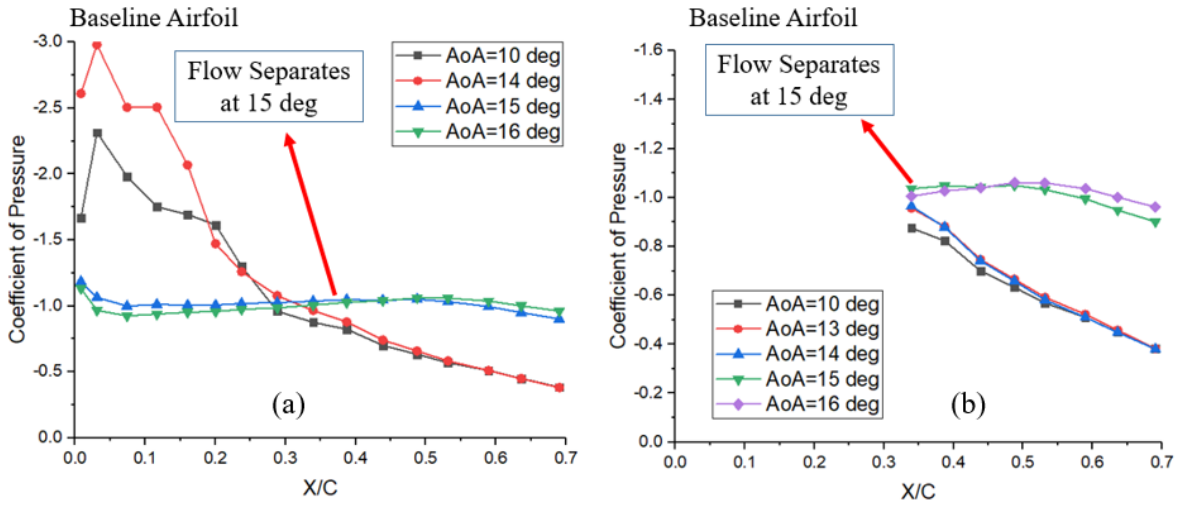

Figure 21. Pressure distribution for the (a) upper surface under Re= 92,000, and (b) lower surface under Re= 92,000.

3.3.2. Flexible leading-edge airfoil pressure distribution

The pressure distribution was investigated for the flexible leading-edge airfoil to estimate its static stall angle under Reynolds number- 46,000 and 92,000. The results were plotted in Figure 22 with the results from baseline airfoil for the comparison (Figures 20-21). It can be observed from Figure 22 that the airfoil is likely to experience the static stall at the angle of 14°. However, the baseline airfoil is likely to experience the stall at an earlier incident angle- 13°. In terms of the coefficient of pressure on the lower surface (with flexible leading edge) of these two airfoils, it can be found from the Figure 22 that the flexible leading-edge airfoil was not likely to experience the static stall until 16°; in contrast, the baseline airfoil meet the stall much earlier at 13°, which indicates that the flexible surface helps delay the flow separation. With the increase of the Reynolds number, the performance difference between the flexible leading-edge airfoil and the baseline airfoil was more significant. For the Figure 23, the flexible leading-edge airfoil did not stall until the angle of attack reached at 17° which is 2° larger than that of the baseline airfoil. It can be found that the flexible airfoil delayed the static stall until 18° due to the influence of the flexible leading-edge portion; in contrast, the baseline airfoil stalled as early as 15°.

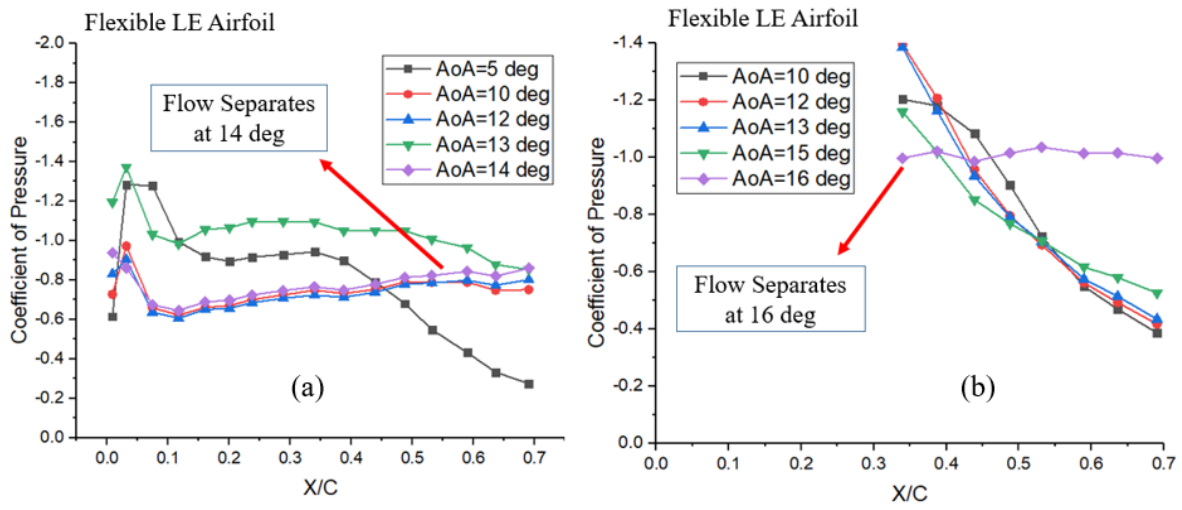

Figure 22. Pressure distribution of the flexible leading-edge airfoil on (a) rigid surface under Re= 46,000, and (b) flexible surface under Re= 46,000.

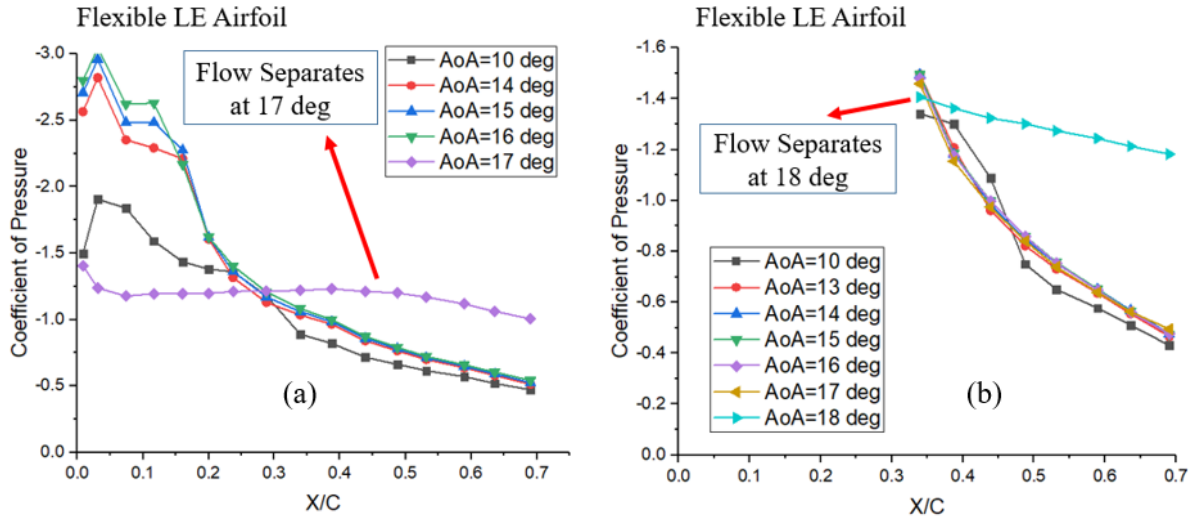

Figure 23. Pressure distribution of the flexible leading-edge airfoil under Re=92,000 on (a) rigid surface, and (b) flexible surface.

3.4. Dynamic pitching scenario

For the dynamic pitching process, the pressure distribution was collected for both upper and lower surface of the baseline airfoil as the baseline result for the further comparison with data from flexible leading-edge airfoil. The pressure was collected at 500 Hz frequency by the DSA pressure scanner. For the dynamic scenario, the dynamic properties were analyzed by the

reduced frequency as discussed in the section 2.3. Three selected reduced frequencies were chosen for the experiment; they are 0.07, 0.1 and 0.15. The pressure distribution was analyzed by plotting the pressure change for the whole procedure on a specific pressure tap. For example, during the analyzation process of the flexible leading-edge experiment, pressure taps #2, 9 and 16 at corresponding chord-wise locations X/C= 0.03, 0.36 and 0.69 were selected to represent the pressure change at the leading edge, midpoint and trailing edge. The results were plotted in the section 3.4 for the comparison with the dynamic results of the flexible leading-edge airfoil model.

The variation of pressure coefficient was investigated for the flexible leading-edge airfoil to investigate its dynamic behavior under the Reynolds number- 92,000. The results were plotted with the results from baseline airfoil for the comparison in the Figure 24. Three pressure taps were selected for analysis as mentioned in the section 3.2. For the Figure 24 (a)-(c), these figures demonstrated the airfoil dynamic performance (pressure coefficient variation) for pressure tap #2 (X/C=0.03, on the rigid side surface) at Re= 92,000 with reduced frequency at 0.07. It can be found that the pressure cycle produced by the flexible leading-edge airfoil is larger than that of the baseline airfoil, which may suggest a higher lift was generated by the flexible leading-edge airfoil during the pitching process. Nevertheless, the maximum coefficient of pressure of the baseline airfoil model could be discovered at a larger angle of attack which is about 25° in (a). The flexible airfoil might experience the decrease of surface pressure at this location at approximately 20°. For both baseline airfoil model and flexible airfoil model, the maximum pressure coefficient would be observed at a larger angle of attack at other pressure taps.

Figure 25 (a)-(c) demonstrates pressure coefficient variations with a reduced frequency of 0.1 under the same Re number. Similarly, it can be found that the pressure cycle produced by the

flexible leading-edge airfoil is larger than that of the baseline airfoil, which may suggest a higher lift was generated during the pitching process. The maximum negative coefficient of pressure of the baseline airfoil model could be discovered at a larger angle of attack which is about 23° in Figure 25 (a). The flexible airfoil might experience the decrease of surface pressure at this location at approximately 17°. For the Figure 26 (a)-(c), it is interesting to note that the flexible leading-edge airfoil experienced dynamic stall about 27 degree; in contrast, the baseline airfoil stalled as early as 19 degree. In this case, the flexible leading-edge structure directly delayed the dynamic stall.

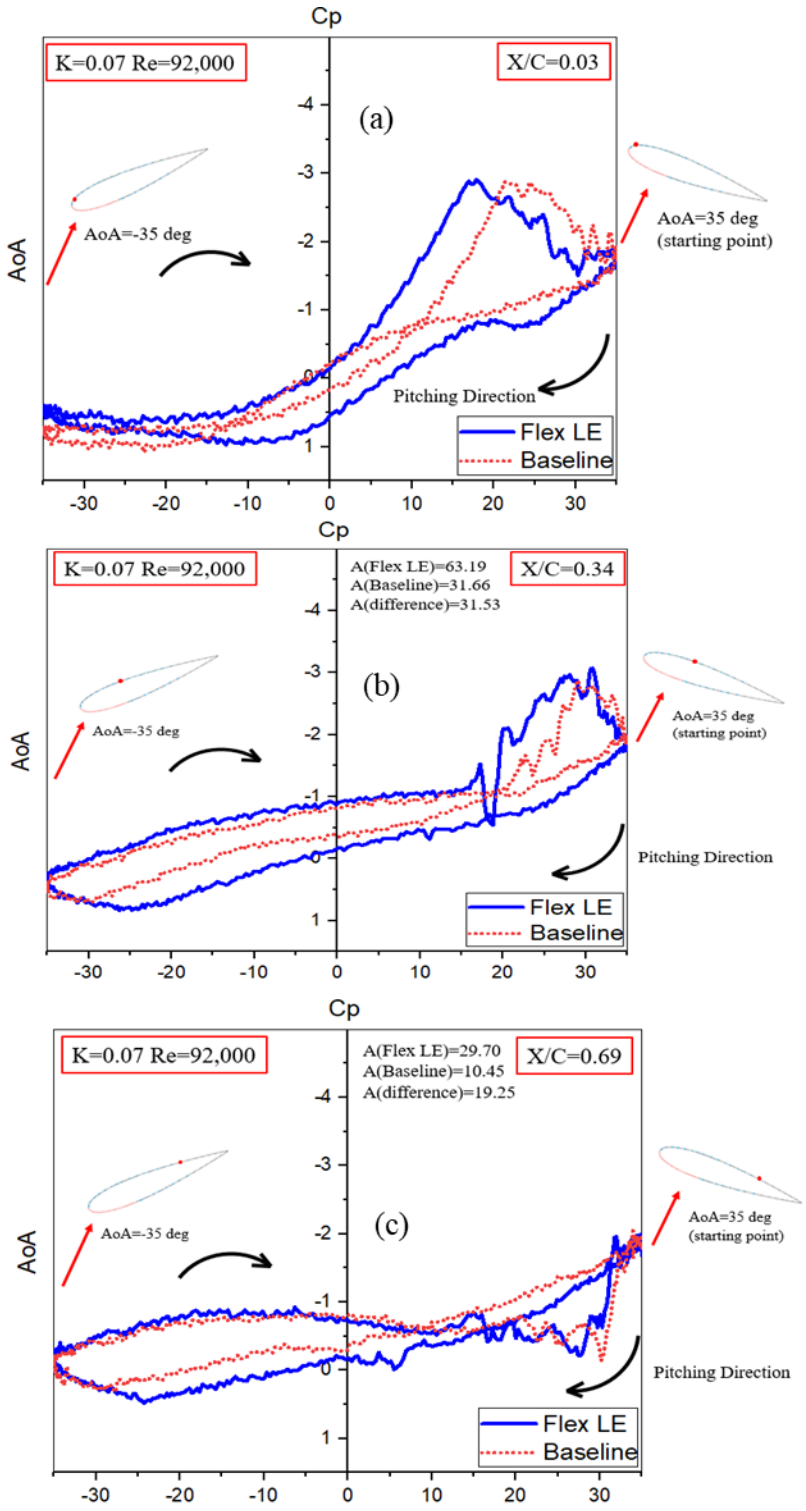

Figure 24. Pressure cycle under Re=92,000 for (a) pressure tap located at X/C=0.03 with k=0.07, (b) pressure tap located at X/C=0.34 with k=0.07, and (c) pressure tap located at X/C=0.69 with k=0.07.

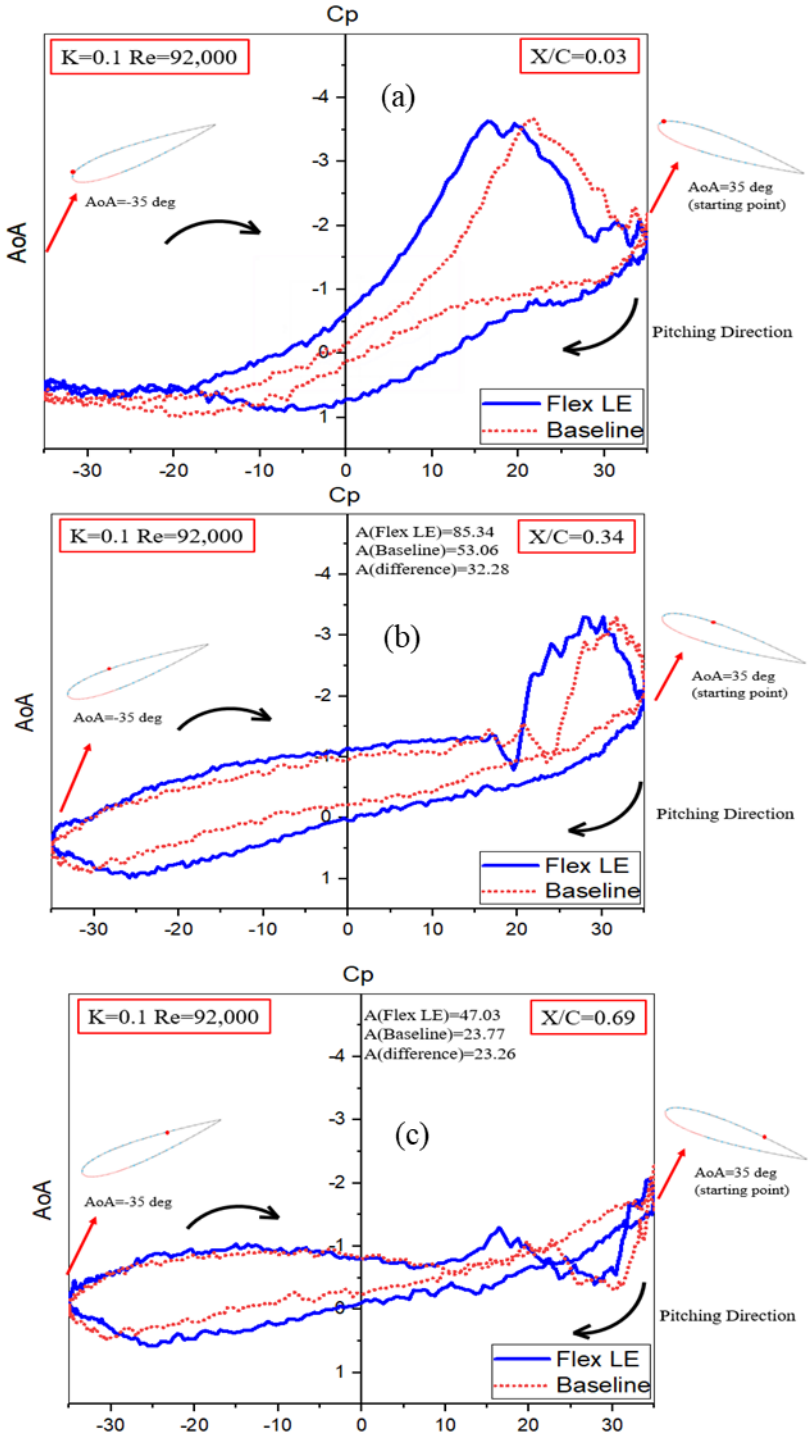

Figure 25. Pressure cycle under Re=92,000 for (a) pressure tap located at X/C=0.03 with k=0.10, (b) pressure tap located at X/C=0.34 with k=0.10, and (c) pressure tap located at X/C=0.69 with k=0.10.

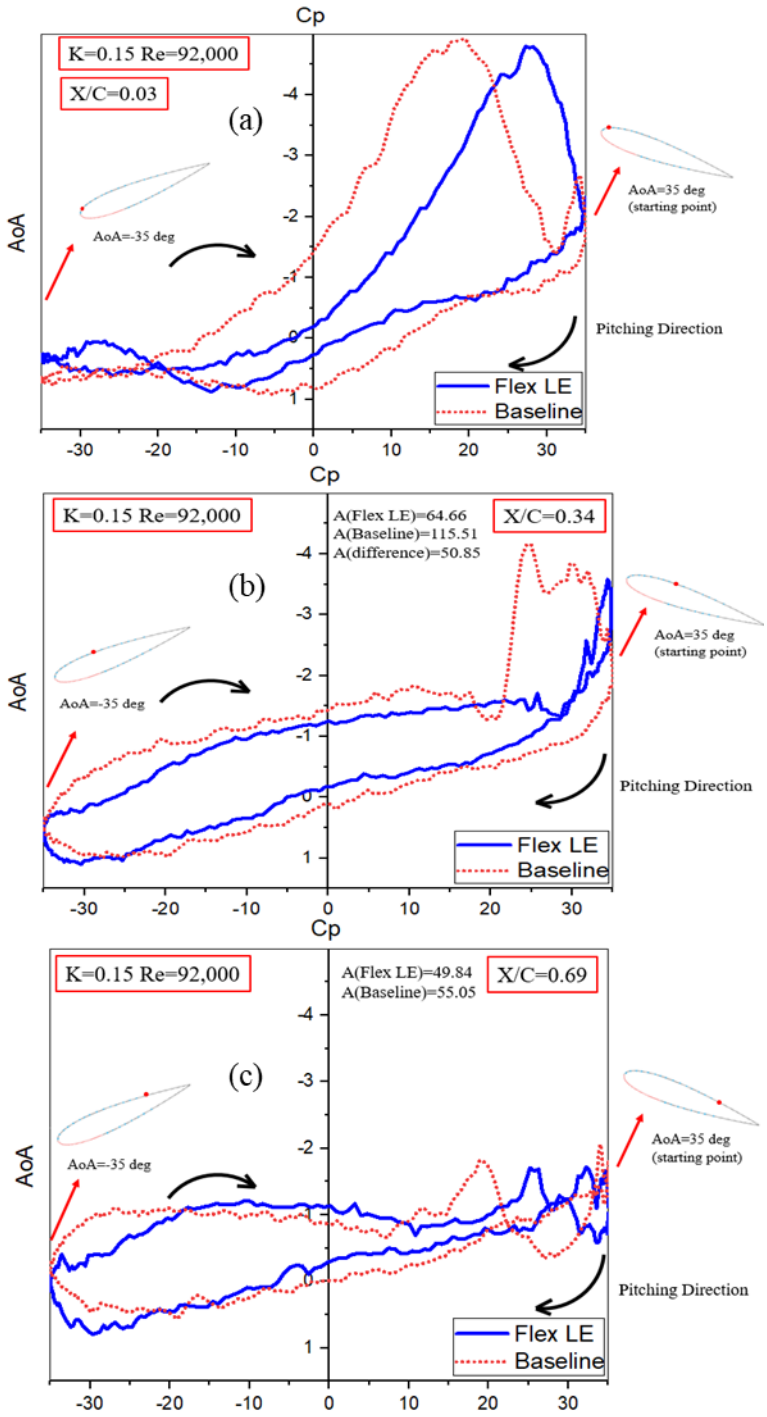

Figure 26. Pressure cycle under Re=92,000 for (a) pressure tap located at X/C=0.03 with k=0.15, (b) pressure tap located at X/C=0.34 with k=0.15, and (c) pressure tap located at X/C=0.69 with k=0.15.

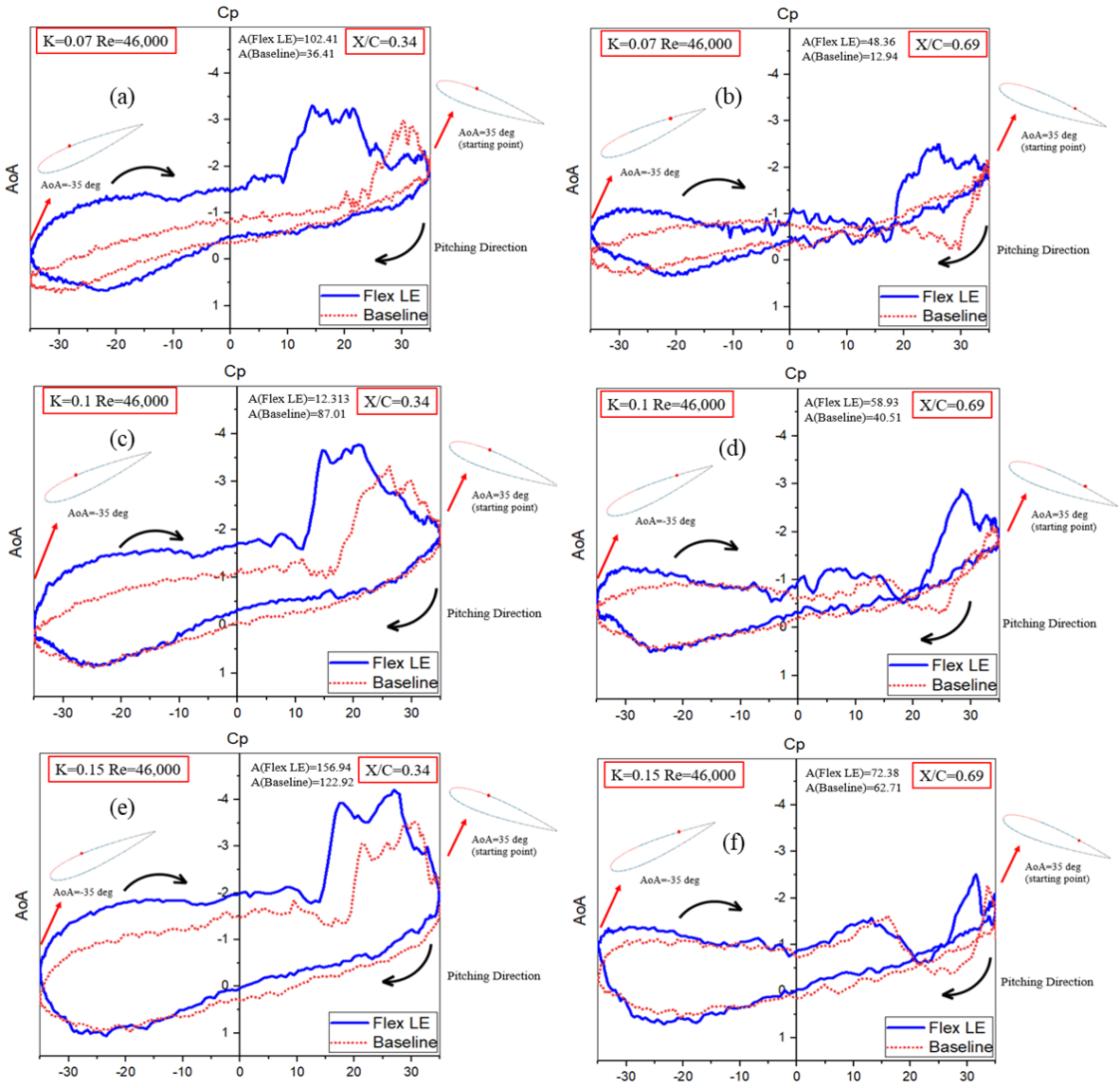

Figure 27. Pressure cycle of the flexible LE airfoil and baseline airfoil on the flexible surface side for (a) pressure tap located at X/C=0.34 with k=0.07, (b) pressure tap located at X/C=0.69 with k=0.07, (c) pressure tap located at X/C=0.34 with k=0.1, (d) pressure tap located at X/C=0.69 with k=0.10, (e) pressure tap located at X/C=0.34 with k=0.15, and (f) pressure tap located at X/C=0.69 with k=0.15.

The Figure 27 (a)-(b) demonstrates the airfoil dynamic performance at a smaller Reynolds number 46,000 for the pressure tap #9 (X/C=0.34) and pressure tap #16 (X/C=0.69) with a reduced frequency of 0.07. Similarly, it can be found that the pressure cycle produced by the flexible leading-edge airfoil is larger than that of the baseline airfoil, which may suggest a higher lift was generated during the pitching process. The maximum negative coefficient of pressure of the baseline airfoil model could be discovered at a larger angle of attack which is about 29° in Figure 27 (d). The flexible airfoil might experience the decrease of surface pressure at this location at approximately 13°. For the Figure 27 (c)-(d), (e)-(f), a similar tendency could be found that the flexible leading-edge structure seems to result in the earlier stall but can generate overall higher lift than the baseline airfoil.

3.5. Flexible leading-edge airfoil visualization analysis

The visualization analysis was employed to understand the qualitative structure deformations associated with the dynamic pitching process. The high-speed camera was used for the image taken. The photos shown in Figure 28 below demonstrate a half cycle of pitching motion where the airfoil starts from -35° to 35° in a flow with Re = 92,000 It can be seen that when the airfoil pitch to an angle larger than 15 °, the flexible structure deformed significantly which is likely to increase the camber of the airfoil, which might explain the increased area of the pressure coefficient loop curve shown in the previous section. This deformation would benefit the improvement of aerodynamic performance to allow the airfoil to adopt more wind energy.

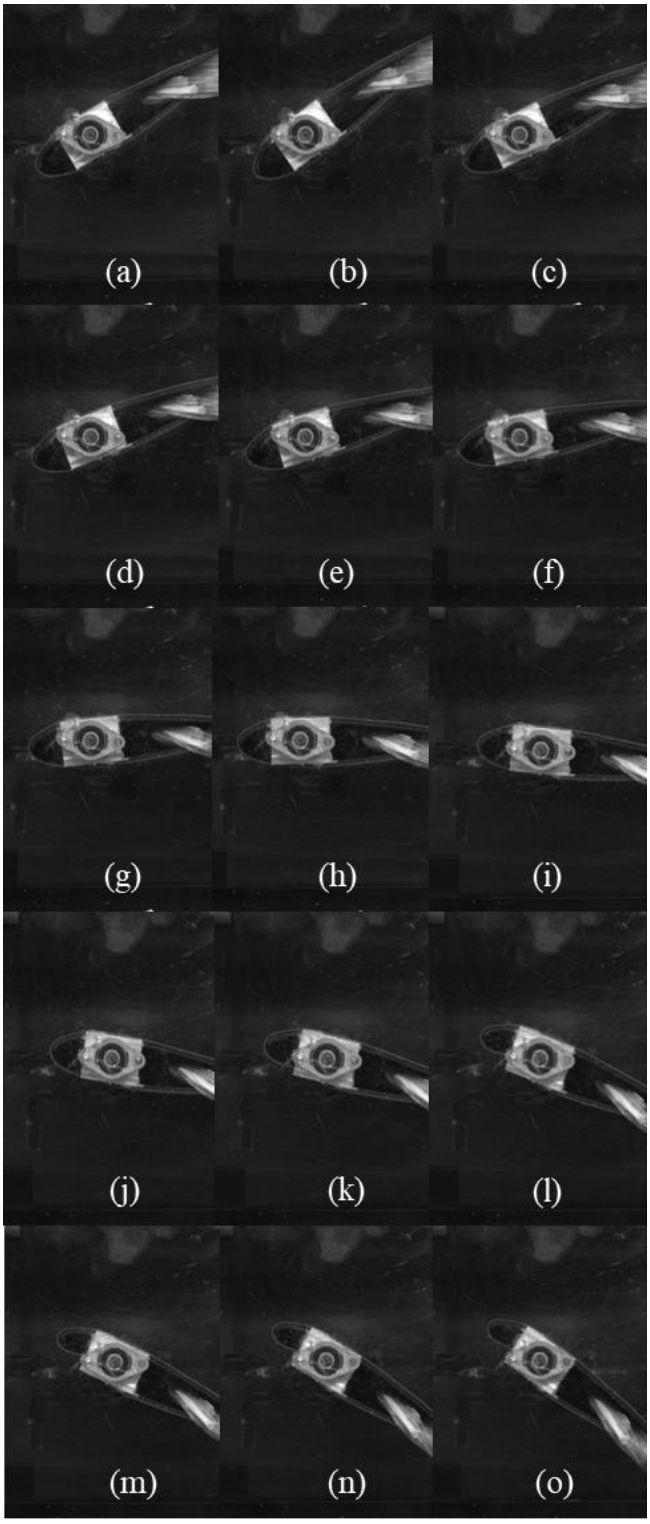

Figure 28. Dynamic pitching motion images of flexible leading-edge airfoil at Re=92,000 at (a) AoA= -35°, (b) AoA= -30°, (c) AoA= -25°, (d) AoA= -20°, (e) AoA= -15°, (f) AoA= -10°, (g) AoA= -5°, (h) AoA= 0°, (i) AoA= 5°, (j) AoA= 10°, (k) AoA= 15°, (l) AoA= 20°, (m) AoA= 25°, (n) AoA= 30°, (o) AoA= 35°.

3.6. Discussion

The flexible leading-edge airfoil contributed to the delay of the static stall which could be observed from the section 3.3. and 3.4. At Re= 46,000, the baseline airfoil experienced static stall as early as 14°; in contrast, the flexible leading-edge airfoil did not experience stall until 15°. A more obvious difference is likely to be found at Re= 92,000, where the baseline airfoil experienced the static stall at 15°. However, the flexible leading-edge structure contributed to a larger stall angle which is 17°.

In terms of the dynamic pitching, the phenomenon became more complex. It could be observed that for a relatively low reduced frequency of 0.07 and 0.1, the flexible leading-edge airfoil is likely to experience an earlier dynamic stall during the pitching process; nevertheless, the overall area enclosed by the pressure coefficient curve of the flexible leading-edge airfoil is larger than that of the baseline airfoil for every test case, which is likely to suggest a higher lift was generated during the process. When k=0.15, a larger stall angle could be found for the flexible leading-edge airfoil than that of the baseline airfoil. A similar tendency could be observed on the pressure coefficient loop (cycle) of a pressure tap on the rigid side surface.

From the images taken for the dynamic pitching motion of flexible leading-edge airfoil at Re= 92,000, an obvious deformation could be observed when the incident angle exceeded 15 degree, which implies that the flexible leading-edge airfoil may generate more lift as it became a high-cambered airfoil.

4. LEADING-EDGE ROUGHNESS AIRFOIL

4.1. Introduction

This chapter will describe the experimental investigation of the leading-edge roughness airfoil model which is modified from a baseline NACA 0018 airfoil. In section 4.2, the design factors of the airfoil are given. The aerodynamic behaviors of the baseline airfoil and two leading-edge roughness airfoils (Grit 60 and Grit 100 roughness applied airfoil) are analyzed from section 4.3 to 4.6 for both steady flow condition and dynamic pitching condition. Finally, section 4.7 presents some discussions on the performance of the leading-edge roughness structure and gives some recommendations which contribute to a better leading-edge roughness airfoil model.

4.2. Leading-edge roughness airfoil model

Figure 29 shows the schematic of the leading-edge roughness airfoil model tested in the present study. The leading-edge roughness airfoil was completed by modifying the NACA 0018 airfoil by covering the 35% of both the upper and lower leading-edge surface. To achieve the leading-edge roughness, some ideas, such as 3D printed dimples and painted small particle, were come into consideration. The final decision for the roughness candidate was made to be the flexible sandpaper. Grit 60 and Grit 100 3M pro grade ultra-flexible sanding papers were chosen for the experiment as they fulfilled the requirement of distributed roughness (shown in the Figure 30). The roughness sizes for the Grit 60 and Grit 100 are 269 micrometers and 162 micrometers, respectively. These sandpapers were tightly stick to the airfoil surface and the trail edge was covered by smooth material to prevent the gap between the roughness area and the non-roughness area.

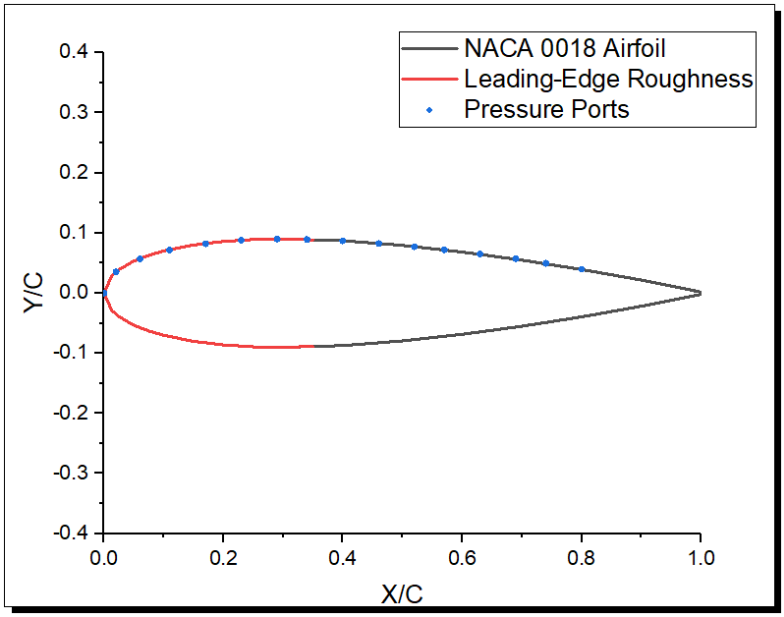

Figure 29. Schematic of leading-edge roughness airfoil.

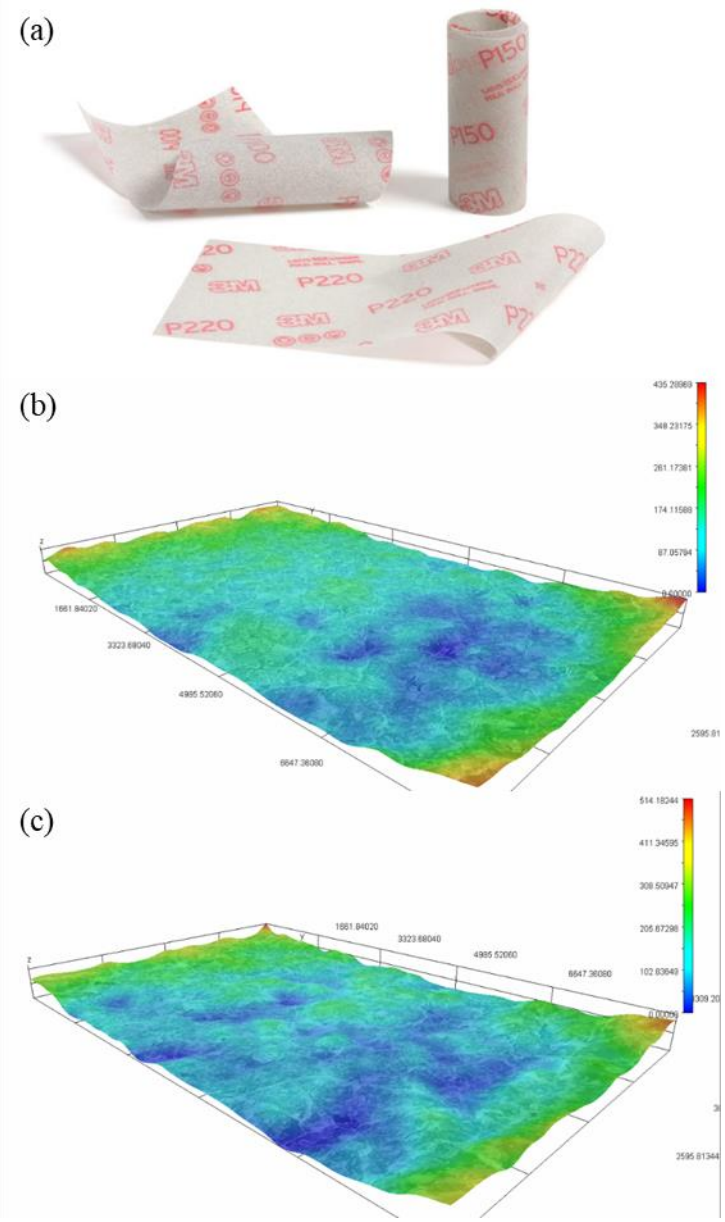

Figure 30. Sandpaper profile of (a) 3M pro grade ultra-flexible sandpaper, (b) Grit 100 roughness surface, and (c) Grit 60 roughness surface.

4.3. Lift coefficient analysis for roughness airfoils: steady state

The lift coefficient was calculated to determine the aerodynamic performance changes of the baseline airfoil, leading-edge Grit60 roughness airfoil and leading-edge Grit100 roughness airfoil under steady flow situation in different angle of attack ranging from 0 to 16 degree. The lift was analyzed by integrating the surface pressure over the airfoil which is measured by the

DSA pressure scanner indicated in the Section 2.3. From the Figure 31 below, it can be seen that the leading-edge Grit 100 roughness airfoil model has the best performance among all three airfoil models where the Grit 60 roughness airfoil has the least performance on delaying the static stall under higher Reynold's number condition. For the lower Reynold's number condition, the Grit 100 roughness airfoil does not experience the stall until the angle of attack increased to 14 degree. The baseline airfoil has the earliest stall at 12 which is 1 degree earlier than the Grit 60 roughness airfoil. In terms of the higher Reynold's number situation, the Grit 100 roughness airfoil does not suffer the stall until 15 degree, which is 1 degree delayed than the stall angles of baseline and Grit 60 airfoil model.

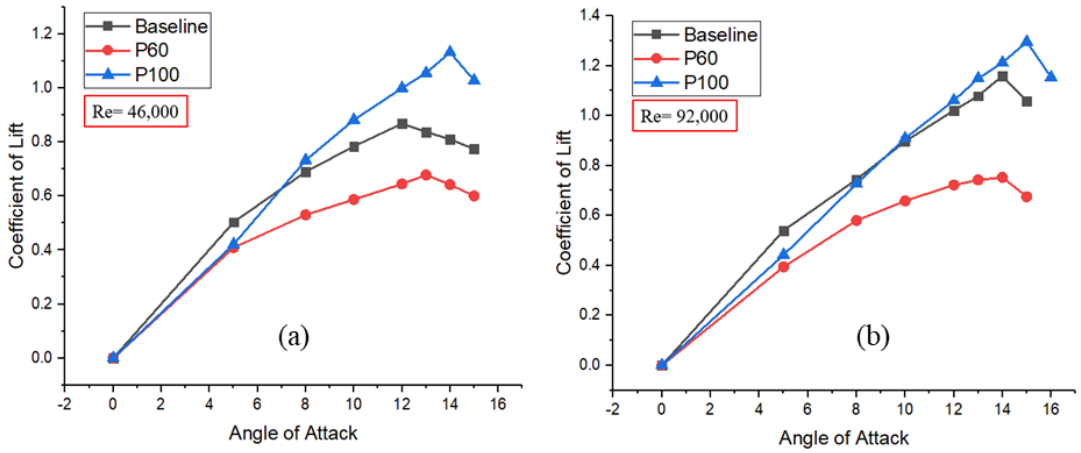

Figure 31. Coefficient of lift for three airfoil models at (a) Re=46,000 and (b) Re=92,000.

4.4. Pressure measurement of leading-edge roughness airfoil

The pressure distribution was investigated for the leading-edge roughness airfoil (Grit 60 and Grit 100) to investigate its dynamic behavior under the Reynolds number- 92,000. The results were plotted with the results from baseline airfoil for the comparison in the Figure 32. For the Figure 32 (a)-(c), these figures demonstrated the airfoil dynamic performance for the pressure tap #2 (X/C=0.02) with the Reynold's number at 92,000 and reduced frequency at 0.07. It could be observed that the Grit 60 leading-edge roughness airfoil seems to have the smallest pressure

cycle which is likely to indicate the least lift it may be generated during the process. The pressure cycles generated by the baseline airfoil and the Grit 100 roughness airfoil are similar, but the pressure cycles of Grit 100 roughness airfoil were slightly larger, which may indicate a higher lift was generated by the Grit 100 LE roughness airfoil. Grit 100 leading-edge roughness airfoil also has its maximum pressure of coefficient happened at a larger angle of attack than the baseline airfoil, which indicated a delayed dynamic stall. In Figure 33 (a), it is more obvious that, airfoil covered by Grit 100 roughness is likely to have a larger stall angle than the baseline airfoil and Grit 60 roughness covered airfoil. However, three airfoils' performance are similar when k=0.15 (seen in Figure 34). The phenomena mentioned above would demonstrate that the Grit 100 roughness applied on the leading-edge of the NACA 0018 airfoil is possible to have the best performance and contribute to the delay of dynamic stall in this experiment when k =0.7 and 0.1.

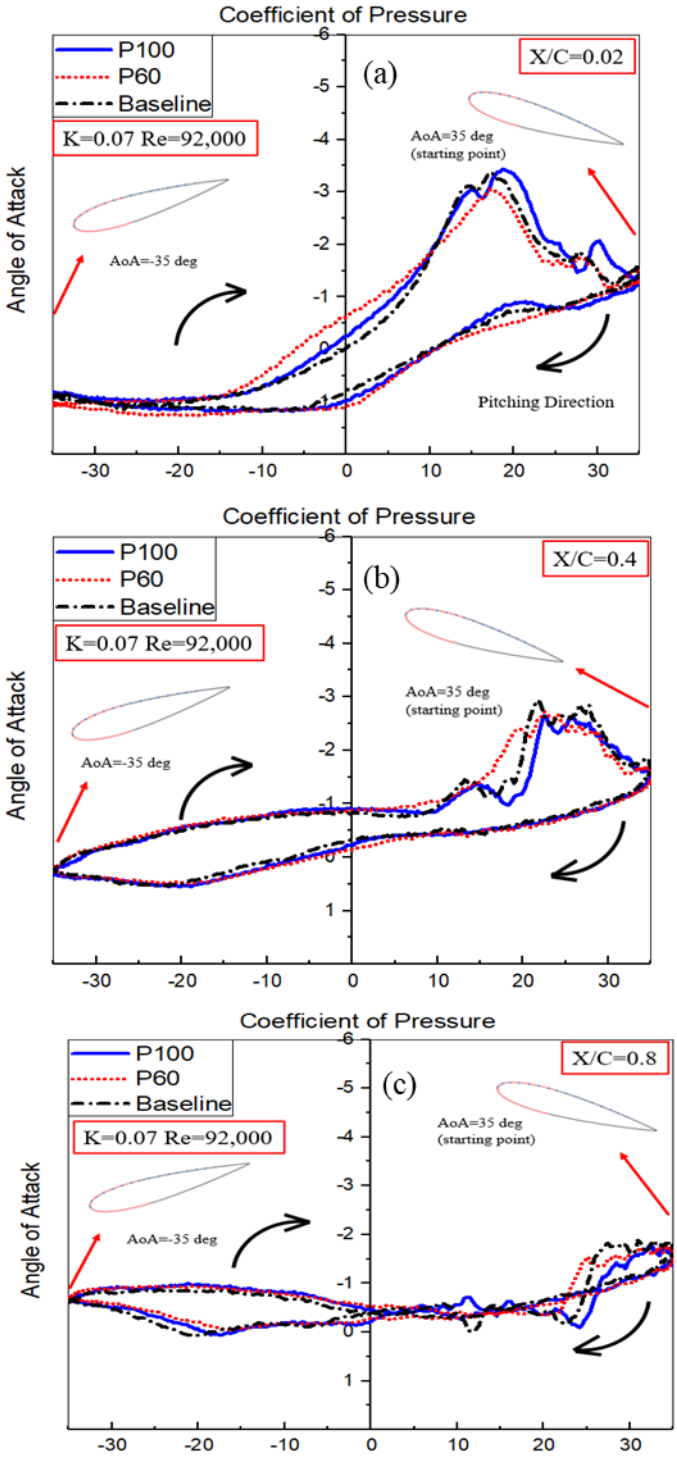

Figure 32. Pressure cycle under Re= 92,000 for (a) pressure tap located at X/C=0.02 with k=0.07, (b) pressure tap located at X/C=0.4 with k=0.07, and (c) pressure tap located at X/C=0.8 with k=0.07.

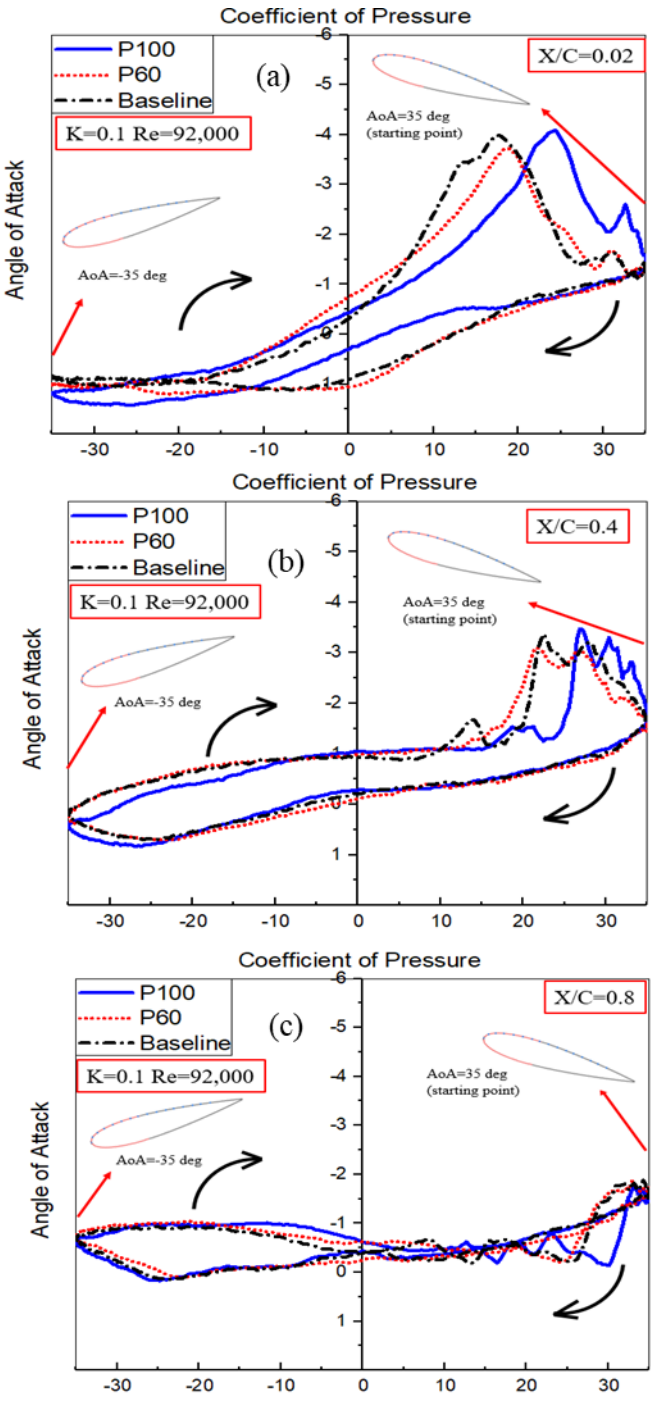

Figure 33. Pressure cycle under Re= 92,000 for (a) pressure tap located at X/C=0.02 with k=0.10, (b) pressure tap located at X/C=0.4 with k=0.10, and (c) pressure tap located at X/C=0.8 with k=0.10.

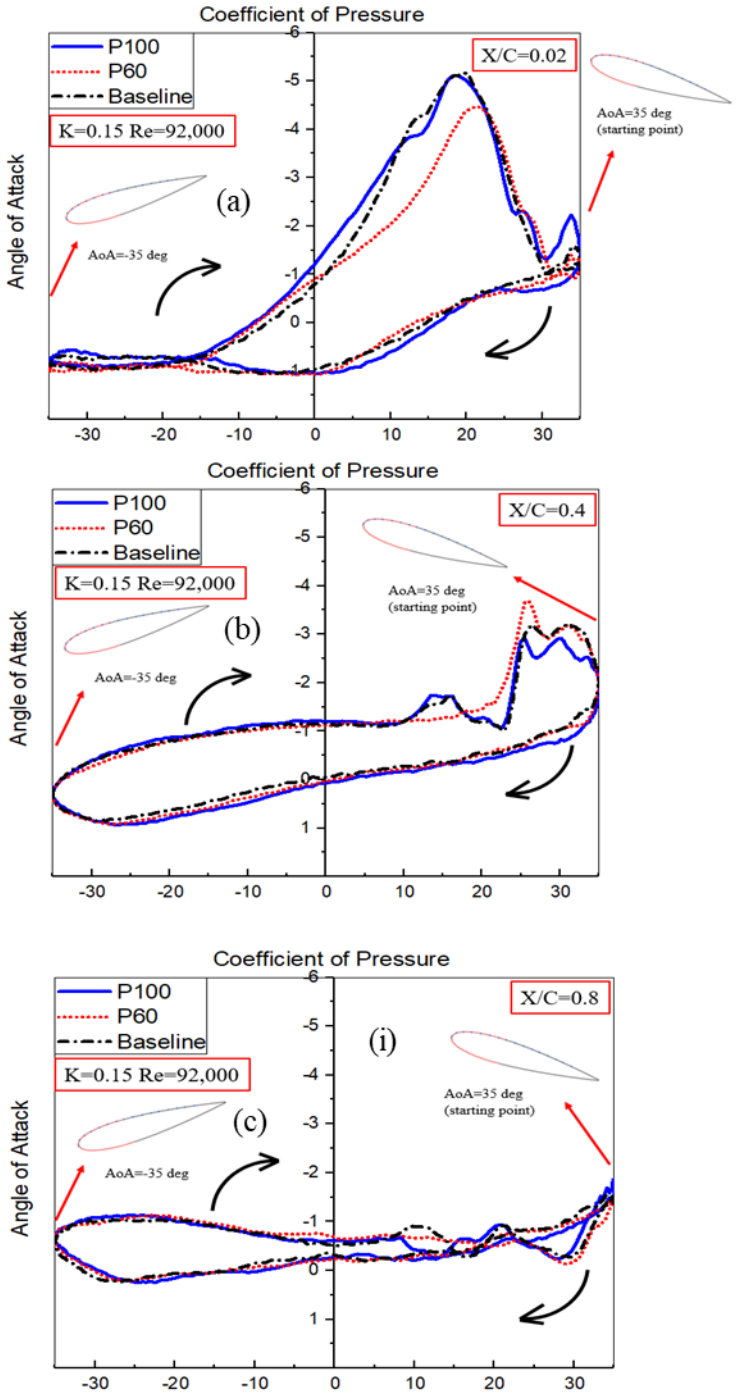

Figure 34. Pressure cycle under Re= 92,000 for (a) pressure tap located at X/C=0.02 with k=0.15, (b) pressure tap located at X/C=0.4 with k=0.15, and (c) pressure tap located at X/C=0.8 with k=0.15.

4.5. Velocity fluctuation in the wake – baseline airfoil

The instantaneous velocity was measured for the baseline airfoil at midpoint which is one- chord length away from the airfoil. The velocity measurements were performed for three different reduced frequencies; k= 0.07, 0.1 and 0.15. The pattern of the variation of velocity did not change rapidly with the increase of reduced frequency; hence, only the period for k=0.7 case and its corresponding turbulence intensity is shown in the Figure 35 below.

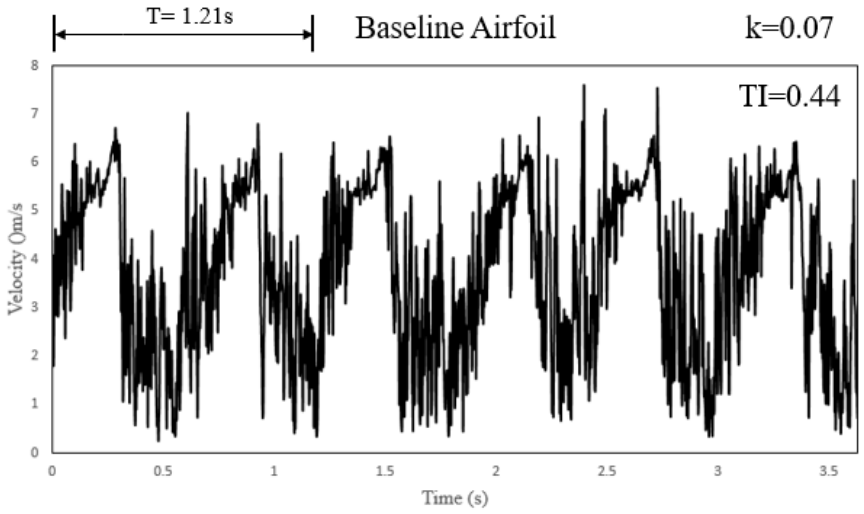

Figure 35. Instantaneous velocity for baseline airfoil at Re= 46,000 at k= 0.07.

4.6. Velocity fluctuation in the wake –leading-edge roughness airfoil

The instantaneous velocity was measured for the leading-edge Grit 60 and Grit 100 roughness airfoil at midpoint as well. The velocity measurements were performed for the reduced frequencies: k= 0.07. The period for each motion and its corresponding turbulence intensity were indicated in the Figure 36 and Figure 37 below. It can be observed that the turbulence intensity increased from 44% (baseline airfoil) to 51% (Grit 60 roughness airfoil) and to 52% (Grit 100 roughness airfoil).

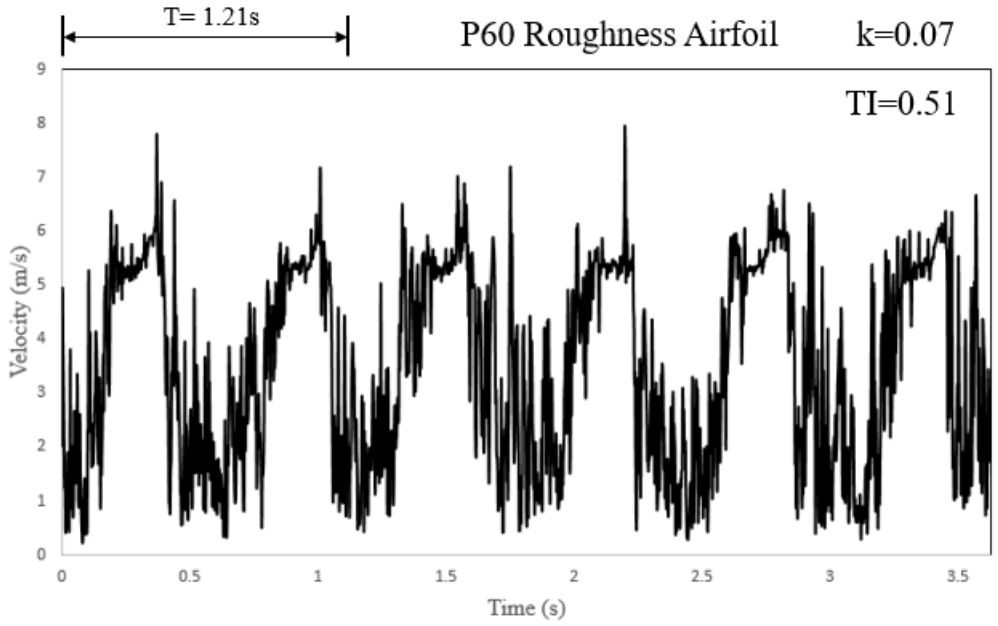

Figure 36. Instantaneous velocity for leading-edge Grit 60 roughness airfoil at Re= 46,000 at k=0.07.

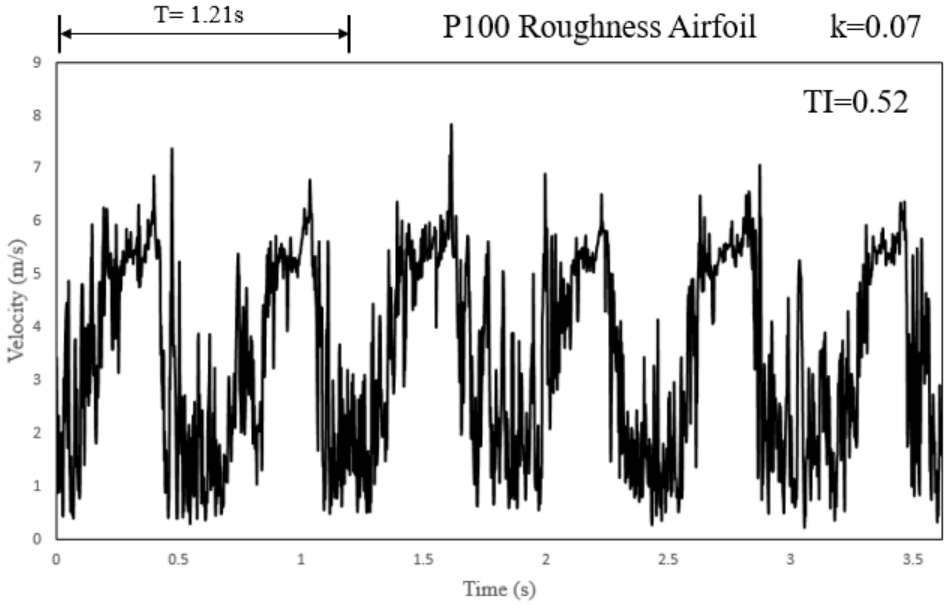

Figure 37. Instantaneous velocity for LE Grit 100 roughness airfoil at Re= 46,000 at k= 0.07.

4.7. Discussion

In this chapter, the effect of leading-edge roughness was investigated for its influence on altering the aerodynamic performance. In the aspect of the steady flow condition, the lift curve was presented to demonstrate the positive effect of the leading-edge Grit 100 roughness on delay the static stall. At Re= 46,000, airfoil covered by the leading-edge Grit 100 roughness experienced the stall at 14 degree which is delayed by 1 degree than the Grit 60 roughness airfoil and by 2 degree than that of the baseline airfoil. The Grit 100 roughness airfoil also has the maximum coefficient of lift during this process. At Re= 92,000, it is similar that the Grit 100 roughness delayed the static stall to 15 degree; meanwhile, the baseline airfoil and the Grit 60 roughness airfoil experienced the stall at 14 degree.

For the dynamic process, the leading-edge Grit 100 roughness airfoil has a similar pressure cycle with the baseline airfoil at k=0.07 and 0.15. However, at k=0.1, the Grit 100 roughness airfoil experienced dynamic stall at a larger incident angle than that of the baseline and Grit 60 roughness airfoil.

From the velocity data in the section 4.5 and 4.6, it seems like that the leading-edge roughness does not have great impact on the large-scale flow structure in the wake of the airfoils. From the Figure 35, 36 and 37, the pattern of the velocity fluctuations was similar among all cases. However, the leading-edge roughness does increase the turbulence intensity of the wake flow during the pitching motion.

5. CONCLUSION

5.1. Conclusion

The goal of this thesis was to investigate the performance improvements of modified leading-edge structures on NACA 0018 airfoil under steady flow condition and dynamic pitching condition. In the experiments the modified leading-edge structure airfoils were tested in terms of pressure distribution, velocity measurement and visualization measurement and compared to the baseline configurations.

For the steady flow condition, both modified leading-edge structures (flexible leading-edge and fine leading-edge roughness) presented their significant impact on improving the aerodynamic performance by delaying the static stall angle compared to the baseline airfoil. Larger size roughness airfoil, however, does not have an obvious improvement on its aerodynamic behavior.

For the dynamic pitching process, the performance of each airfoil was evaluated by plotting their pressure cycle during the pitching motion. For the modified leading-edge structures, a similar tendency could be found. Both airfoil models induced an earlier dynamic stall during the process but have a larger overall pressure cycle than that of the baseline airfoil, which is likely to indicate a higher overall lift was generated during the process. A finer roughness (Grit 100) seems to have a positive impact on improving the aerodynamic behavior of airfoil than the Grit 60 roughness. Images for the flexible leading-edge airfoil performed pitching motion at Re=92,000 visualized the deformation of flexible structures and demonstrated its potential to gain more lift than rigid airfoil due to increased camber during the pitching motion.

Overall, the modified leading-edge structures discussed in this paper would have the potential to enhance the aerodynamic performance of the vertical axis wind turbine to gain a higher lift during rotational operation.

5.2. Uncertainty analysis

In this experiment, the error involved is likely to be classified into two classes: bias error (systematic error) and random error. The bias error is a main error source in this experiment included the error from the dynamic pitching system as it gives approximately ±5% of the uncertainty of the oscillating motion. Hence, the estimated error for the pitching angle is about ± 0.7 degree from its designed angle. During the pressure measurement of dynamic pitching motion, 10 cycles of pitching were performed. However, the first and last pressure cycles were discarded to limit the inaccuracy induced by the stepper motor as it needs to speed up and slow down during the first and last pitching cycles. For the uncertainty during the pressure measurement, a bias error is expected to be 0.05% with a 1.75% of the random error. Hence, the total error can be analyzed to be 1.75%. For the velocity measurements, a 0.01% bias error could be observed from CTA hot wire anemometer with a 6.75% of random error. A total 6.75% error is calculated for the velocity measurement portion. The uncertainty analysis is also applied for the pressure cycle. The bias error is determined to be 6% with a 2% of random error.

5.3. Recommendation

The investigation of the passive flow control mechanisms and their impact on the flow fields is very important to improve the aerodynamic performance of vertical axis wind turbines. As the research led to some important conclusions, it also gave rise to new questions and research possibilities. Based on the finding in this thesis, some recommendations could be made for the future research:

1. More roughness sizes should be involved to investigate the leading-edge roughness effects on the aerodynamic characteristics.

2. Advance flow diagnostics, such as PIV (Particle Image Velocimetry) technique, could be used to capture the instantaneous flow fluid with high speed imaging to observe the vortex structure variations during dynamic pitch process.

3. It is recommended to use the metal to construct the airfoil to have a thin layer of the surface. The pressure taps could be applied on both airfoil surfaces for the calculation of coefficient of lift.

REFERENCES

[1] American Wind Energy Association, "Wind Energy Facts at a Glance," Available: https://www.awea.org/wind-101/basics-of-wind-energy/wind-facts-at-a-glance, Accessed on: May 15, 2020.

[2] B.D. Hoen, J.E. Diffendorfer, J.T. Rand, et al., "United States Wind Turbine Database." U.S. Geological Survey, 2018, doi: 10.5066/F7TX3DN0.

[3] A. Hemami, *Wind Turbine Technology*. Australia: Delmar, Cengage Learning, 2012.

[4] U.S. Department of Energy, "History of U.S. Wind Energy," Available: https://www.energy.gov/eere/wind/history-us-wind-energy, Accessed on: May 15, 2020.

[5] C. Ingraham, "Every one of America's 57,636 wind turbines, mapped," *Washington Post*. Available: https://www.washingtonpost.com/news/wonk/wp/2018/05/11/every-one-of-americas-57636-wind-turbines-mapped/, Accessed on: May 15, 2020.

[6] N. El Bassam, P. Maegaard, and M. L. Schlichting, "Chapter Eight - Wind Energy," in *Distributed Renewable Energies for Off-Grid Communities*, N. El Bassam, P. Maegaard, and M. L. Schlichting, Eds. Elsevier, 2013, pp. 111–123.

[7] Renewable Energy World, "Offshore Use of Vertical-axis Wind Turbines Gets Closer Look," Available: https://www.renewableenergyworld.com/2012/08/08/offshore-use-of-vertical-axis-wind-turbines-gets-closer-look/, Accessed on: Oct. 14, 2019.

[8] H. M. Dodd, T. D. Ashwill, D. Berg, M. E. Ralph, W. A. Stephenson, and P. Veers, "Test results and status of the DOE/Sandia 34-m VAWT Test Bed," 1989. Accessed on May 15, 2020.

[9] H. M. Dodd, T. D. Ashwill, D. E. Berg, M. E. Ralph, W. A. Stephenson, and P. S. Veers, "Test results and status of the DOE/Sandia 34-m VAWT Test Bed," Sandia National Labs., Albuquerque, NM (USA), SAND-89-1535C; CONF-8909217-1, Jan. 1989. Available: https://www.osti.gov/biblio/5491670, Accessed on: May 15, 2020.

[10] Y. Zhang, J. Zhao, B. Grabrick, B. Jacobson, A. Nelson, and J. Otte, "Dynamic response of three floaters supporting vertical axis wind turbines due to wind excitation," *Journal of Fluids and Structures*, vol. 80, pp. 316–331, Jul. 2018, doi: 10.1016/j.jfluidstructs.2018.04.003.

[11] R. Howell, N. Qin, J. Edwards, and N. Durrani, "Wind tunnel and numerical study of a small vertical axis wind turbine," *Renewable Energy*, vol. 35, no. 2, pp. 412–422, Feb. 2010, doi: 10.1016/j.renene.2009.07.025.

[12] Z. Zhao *et al.*, "Study on variable pitch strategy in H-type wind turbine considering effect of small angle of attack," *Journal of Renewable and Sustainable Energy*, vol. 9, no. 5, p. 053302, Sep. 2017, doi: 10.1063/1.4989795.

[13] P. Liu and B. Veitch, “Design and optimization for strength and integrity of tidal turbine rotor blades,” *Energy*, vol. 46, no. 1, pp. 393–404, Oct. 2012, doi: 10.1016/j.energy.2012.08.011.

[14] W. Mccroskey, L. Carr, and K. Mcalister, “Dynamic stall experiments on oscillating airfoils,” *13th Aerospace Sciences Meeting*, 1975.

[15] T. C. Corke and F. O. Thomas, “Dynamic Stall in Pitching Airfoils: Aerodynamic Damping and Compressibility Effects,” *Annual Review of Fluid Mechanics*, vol. 47, no. 1, pp. 479–505, 2015, doi: 10.1146/annurev-fluid-010814-013632.

[16] L. Carr, “Dynamic stall progress in analysis and prediction,” *12th Atmospheric Flight Mechanics Conference*, 1985.

[17] J. Hrynuk, “The effects of leading edge roughness on dynamic stall,” presented at the APS Division of Fluid Dynamics Meeting Abstracts, Nov. 2016, p. D6.005, Available: http://adsabs.harvard.edu/abs/2016APS..DFD.D6005H, Accessed on: Oct. 15, 2019.

[18] S. Yarusevych, P. E. Sullivan, and J. G. Kawall, “On vortex shedding from an airfoil in low-Reynolds-number flows,” *Journal of Fluid Mechanics*, vol. 632, pp. 245–271, Aug. 2009, doi: 10.1017/S0022112009007058.

[19] A. Thu, “Dynamic Stall Vortex Formation of OA-209 Airfoil at Low Reynolds Number,” *Int’l Journal of Mechanical, Industrial Science and Engineering*, Jan. 2014.

[20] H. Mai, G. Dietz, W. Geißler, K. Richter, J. Bosbach, H. Richard, and K. D. Groot, “Dynamic Stall Control by Leading Edge Vortex Generators,” *Journal of the American Helicopter Society*, vol. 53, no. 1, p. 26, 2008.

[21] G. P. Corten and H. F. Veldkamp, “Insects can halve wind-turbine power,” *Nature*, vol. 412, no. 6842, pp. 41–42, Jul. 2001, doi: 10.1038/35083698.

[22] L. N. Cattafesta and M. Sheplak, “Actuators for Active Flow Control,” 2011, doi: 10.1146/annurev-fluid-122109-160634.

[23] P. NithinHegde, A. Tiwari, Paul, and A. Jain, “Investigation of Flow Control in Transition Air-Intake using Synthetic Jet Actuators,” Jul. 2013.

[24] D. Jansen, “Passive Flow Separation Control on an Airfoil-Flap Model: The Effect of Cylinders and Vortex Generators,” 2012, Available: https://repository.tudelft.nl/islandora/object/uuid%3A26809f76-fe8e-4486-b992-d6ea0f08963b, Accessed on: May 15, 2020.

[25] L. Gao, Y. Liu, S. Han, and J. Yan, “Aerodynamic performance of a blunt trailing-edge airfoil affected by vortex generators and a trailing-edge wedge,” in *3rd Renewable Power Generation Conference (RPG 2014)*, Sep. 2014, pp. 1–6, doi: 10.1049/cp.2014.0917.

[26] H. Mueller-Vahl, G. Pechlivanoglou, C. N. Nayeri, and C. O. Paschereit, “Vortex Generators for Wind Turbine Blades: A Combined Wind Tunnel and Wind Turbine Parametric Study,” presented at the ASME Turbo Expo 2012: Turbine Technical Conference and Exposition, Jul. 2013, pp. 899–914, doi: 10.1115/GT2012-69197.

[27] D. Micallef, R. Farrugia, T. Sant, and P. Mollicone, “An aerodynamic study on flexed blades for VAWT applications,” *J. Phys.: Conf. Ser.*, vol. 555, p. 012073, Dec. 2014, doi: 10.1088/1742-6596/555/1/012073.

[28] W. Liu and Q. Xiao, “Investigation on Darrieus type straight blade vertical axis wind turbine with flexible blade,” *Ocean Engineering*, vol. 110, pp. 339–356, Dec. 2015, doi: 10.1016/j.oceaneng.2015.10.027.

[29] D. W. MacPhee, “Flexible Blade Design for Wind Energy Conversion Devices,” UC San Diego, 2014.

[30] D. H. Zeiner-Gundersen, “A novel flexible foil vertical axis turbine for river, ocean, and tidal applications,” *Applied Energy*, vol. 151, pp. 60–66, Aug. 2015, doi: 10.1016/j.apenergy.2015.04.005.

[31] A. Abdel-Rahman and W. Chakroun, “Surface roughness effects on flow over aerofoils,” *Wind Engineering*, vol. 21, pp. 125–137, Jan. 1997.

[32] W. Chakroun, I. F. Almesri, and S. Al-Fahad, “Effect of Surface Roughness on the Aerodynamic Characteristics of a Symmetrical Airfoil,” *eScholarship*, 2004. Available: https://www.semanticscholar.org/paper/Effect-of-Surface-Roughness-on-the-Aerodynamic-of-a-Chakroun-Almesri/b798655665c31d285747311fb35902e04276eb4e#extracted, Accessed on: May 15, 2020.

[33] K. Gharali, E. Gharaei, M. Soltani, and K. Raahemifar, “Reduced frequency effects on combined oscillations, angle of attack and free stream oscillations, for a wind turbine blade element,” *Renewable Energy*, vol. 115, pp. 252–259, Jan. 2018, doi: 10.1016/j.renene.2017.08.042.